INFORMATION TO USERS

This manuscript has been reproduced from the microfilm master. UMI films the text directly from the original or copy submitted. Thus, some thesis and dissertation copies are in typewriter face, while others may be from any type of computer printer.

The quality of this reproduction is dependent upon the quality of the copy submitted. Broken or indistinct print, colored or poor quality illustrations and photographs, print bleedthrough, substandard margins, and improper alignment can adversely affect reproduction.

In the unlikely event that the author did not send UMI a complete manuscript and there are missing pages, these will be noted. Also, if unauthorized copyright material had to be removed, a note will indicate the deletion.

Oversize materials (e.g., maps, drawings, charts) are reproduced by sectioning the original, beginning at the upper left-hand corner and continuing from left to right in equal sections with small overlaps. Each original is also photographed in one exposure and is included in reduced form at the back of the book.

Photographs included in the original manuscript have been reproduced xerographically in this copy. Higher quality 6" x 9" black and white photographic prints are available for any photographs or illustrations appearing in this copy for an additional charge. Contact UMI directly to order.

RICE UNIVERSITY

Photoluminescence of Crystalline Thin Film C_{60}
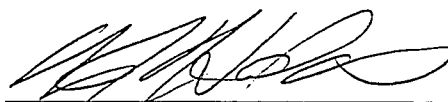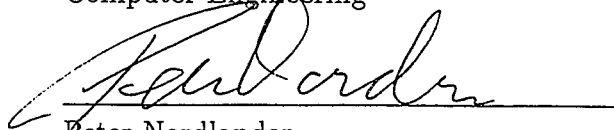
by

Phillip M. Pippenger

A THESIS SUBMITTED
IN PARTIAL FULFILLMENT OF THE
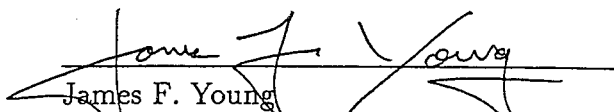REQUIREMENTS FOR THE DEGREE

Master of Science

APPROVED, THESIS COMMITTEE:

Naomi J. Halas, Director
Associate Professor of Electrical and
Computer Engineering

Peter Nordlander
Associate Professor of Physics

James F. Young
Professor of Electrical and Computer
Engineering

Houston, Texas

March, 1995

UMI Number: 1377043

UMI

300 North Zeeb Road
Ann Arbor, MI 48103

Photoluminescence of Crystalline Thin Film C_{60}

Phillip M. Pippenger

Abstract

A method is described for the growth of high purity crystalline thin film C_{60}. Films grown by this method are analyzed by means of x-ray diffraction, low energy electron diffraction, and photoluminescence. An excimeric model of the processes leading to the observed photoluminescence spectrum is proposed. This model is supported by the locations of spectral features in the photoluminescence spectrum as well as by agreement with the cooling dependence, temperature dependence, and the lack of film thickness dependence of the photoluminescence spectrum. The model is used to explain the observed photoluminescence spectrum of polycrystalline C_{60}.

Acknowledgments

What's a lab without atmosphere? The atmosphere in our lab was provided by: God, Malt Balls Averitt, Flinkas Tunahead Zamboni, Dipanker the Spanker Sarkar, "Rick, that is my sister" Prato, Gregarious Rex, and "Why start now?" Kelly. Although he hasn't been here for a while now, Jay Resh was an invaluble help early on. His down-to-earth point of view was always encouraging, and his tenacity in every aspect of his life is something I can only aspire to.

The development of the theory explored in this work is due solely to discussions with Valery Papanyan, Peter Nordlander, Naomi Halas, and Rick Averitt.

Dr. Nordlander and Dr. Halas must also be thanked, along with Dr. James Young, for their help as members of my thesis committee.

As my research advisor, Dr. Halas has provided guidance, motivation, focus, and funding for my pursuit of the work in this thesis. She is an advisor like no other and is certainly appreciated, more than she realizes, by me and by her other students.

My family has always been a source of great support for me. Tai-ming was always a great little fuzzy listener, and will always have a place in my heart and a picture on my wall.

Hilleory has been a great comfort and encouragement to me in the darker hours and a wonderful friend in good times.

Contents

Illustrations

Introduction

Chapter 1

Introduction and Outline

1.1 Introduction

The production of bulk quantities of C_{60} has allowed for the intense investigation of solid phase C_{60}. Several important studies have revealed the molecular nature of solid C_{60} [1]. However, in order to have a more complete understanding of the structural, electronic, and vibrational properties of solid C_{60}, intermolecular interactions need to be investigated. A more complete description of the bulk characteristics of C_{60} will aid in the understanding of molecular solids in general. In addition, solid C_{60} has many potentially useful applications, many of which will require a more complete elucidation of its physical properties. For example, C_{60} is an excellent optical limiter [2]; it shows promise as a useful nonlinear optical material [3]; polymer-C_{60} heterojunctions have been fabricated [4]; and alkali metal doped C_{60} is superconducting with a relatively high transition temperature [5, 6, 7].

Photoluminescence (PL) is an important method for investigating the properties of solid C_{60}. However, a significant problem with much of the earlier work was the purity

of the C_{60}. Conclusive studies have not been performed, but there are indications that intercalated solvents affect the electronic and structural properties of solid C_{60} [8]. Additionally, the properties of the various fullerenes differ and higher fullerenes may contribute false features to the C_{60} PL spectrum. Higher fullerenes may also affect the spectrum indirectly, through energy coupling mechanisms with the C_{60} molecules, such as energy pooling [9].

There have been many studies which have focussed primarily on the PL spectrum of polycrystalline C_{60}. While these studies have provided useful information about transition energies and luminescence lifetimes, the small domain nature of polycrystalline films leads to significant inhomogeneous broadening of the C_{60} PL features, making definitive peak assignments difficult.

More recently, PL studies have been performed on C_{60} crystallites grown by vacuum sublimation techniques [10]. While these crystallites have a much higher degree of crystallinity than do polycrystalline samples, resulting in more well resolved spectral features, they are still plagued by unpredictable structural anomalies. Electron diffraction studies have shown that samples grown in this manner can contain rotated domains, as well as completely different crystal structures, such as the hexagonal close

packed (HCP) structure, in addition to the face centered cubic (FCC) stucture most prevalent in solid C_{60} [11, 12].

In order to have a greater degree of control over the crystallinity and thickness of our samples, we have developed a process for growing epitaxial thin film crystalline C_{60}. This process produces crystals of high structural integrity with thicknesses as little as a monolayer or as great as several thousand monolayers.

We have observed the photoluminescence spectrum obtained from (111) oriented, epitaxially grown single crystal thin films of solid phase C_{60}. The photoluminescence spectrum obtained from these C_{60} single crystal thin films is highly reproducible, in contrast to the crystallite PL data previously reported [10]. We have developed a simple theoretical model which takes into account enhanced vibronic mixing due to coupling of an excited C_{60} molecule with its nearest neighbor. The model provides an identification for all of the observed spectral features at low temperature, including the relative peak heights, as well as providing agreement for the experimentally observed temperature dependence of the photoluminescence spectrum. Additionally, our model provides accurate assignment of PL peaks observed in polycrystalline films of C_{60}. An additional benefit conferred by the thin film nature of our crystalline samples is that we are able to perform PL studies on films of varying thicknesses. This allows us to

verify the bulk origin of all of the observed peaks in the PL spectrum, contradicting earlier assignments of certain peaks to surface induced transitions [10].

1.2 Properties of C_{60}

As a third stable form of carbon, the fullerenes have generated great interest among engineers and scientists. Because of its symmetry and availability, C_{60} has become the focus of much of this interest.

The atoms of the C_{60} molecule lie on the vertices of a regular truncated icosahedron. NMR studies verify that all atomic sites on the molecule are equivalent. As it is in the icosahedral point group, C_{60} has the highest symmetry found in molecules now known to exist. Symmetry operations for the molecule consist of 12 five-fold axes, 20 three-fold axes, 15 two-fold axes, as well as the identity operation. Accounting for inversion operations, there are a total of 120 symmetry operations in the icosahedral point group. The diameter of the truncated icosahedron upon which the carbon atoms are located is 6.83 Å. The diameter of the C_{60} molecule itself is 10.18 Å taking into account the extent of the π-electron cloud associated with the atoms [13]. Although C_{60} has a HOMO-LUMO (highest occupied molecular orbital— lowest unoccupied molecular orbital) gap of about 1.9 eV, the transition is symmetry forbidden

in the isolated molecule. Due to the closed shell nature of C_{60}, it is expected to be fairly unreactive, although endohedral doping has been observed to alter the reactivity [14], and charge transfer has been observed. In addition, the photo-oxidation and photo-polymerization of C_{60} has been observed [15].

Solid C_{60} has been produced in both crystalline and polycrystalline form. The crystal structure of solid C_{60} at room temperature is face-centered cubic (fcc). This has been determined using x-ray diffraction, neutron diffraction, and electron diffraction, among other techniques. C_{60} is a van der Waals solid in all three dimensions. Graphite is a van der Waals solid in only one dimension, while diamond is covalent in all three dimensions. Thus C_{60} has the highest compressibility of the allotropic forms of carbon. In the room temperature fcc structure, the nearest neighbor center-to-center separation is 10.02 Å. The in-plane spacing normal to the [111] direction is 14.14 Å [16].

There are regions of high electron concentration located at the double bonds between pentagons on the C_{60} molecule. Regions of low electron concentration are located at the centers of the pentagons. C_{60} molecules in the solid rotate freely at room temperature, while at temperatures below 255 K they begin to display an anisotropic nature [17]. Since the molecules are rapidly spinning at room temperature,

coulombic repulsion between regions of high electron concentration has no effect. At temperatures where the spinning motion is restricted, the balls begin to order in such a way that the electrostatic potential between regions of high electron concentration on adjacent molecules is minimized. This corresponds to the so-called P-configuration, where an electron rich double bond is centered in a pentagon of an adjacent molecule. See Fig 1.1 for a plot of the percentage of molecules not occupying the P-configuration as a function of temperature.
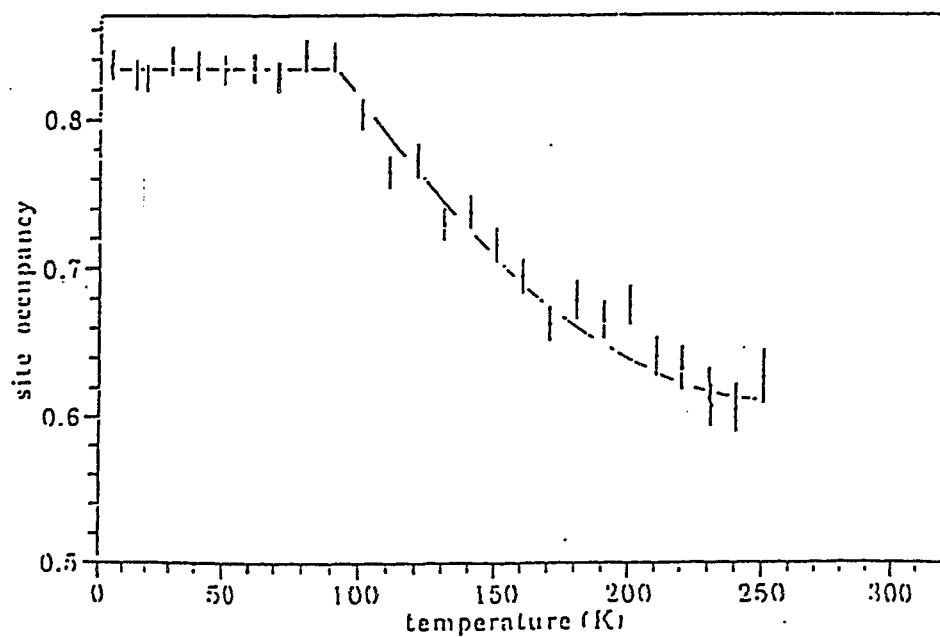
Figure 1.1: Percentage of Molecules Not In the P-configuration as a Function of Temperature after [17]

This leads to the distinction of the four previously indistinguishable molecules in the fcc primitive cell, causing the crystal to become simple cubic. The ratcheting motion of the molecules which begins as the temperature is lowered past 260 K ceases below 90 K as the rotational order is frozen in. At temperatures between these, the fraction of molecules not in the ideal lowest potential energy configuration decreases monotonically with temperature.

While C_{60} is considered to be a semiconductor, the Raman and photoluminescence spectra of solid C_{60} are similar to the spectra for solutions. It can be seen from this that C_{60} is a molecular solid which retains many of the properties of its constituents.

1.3   Thesis Outline

In Chapter 2, the experimental equipment and methods are outlined. The chamber in which C_{60} film growth takes place is described, as well as the methods applied to film growth and low-energy electron diffraction (LEED) analysis. The equipment used in the X-ray diffraction study is briefly described. The latter part of Chapter 2 is devoted to the experimental setup used in the optical studies.

Chapter 3 gives both a theoretical description of LEED and a summary of the information we obtained from LEED studies of the Sb/C_{60} system. The first section

gives the background necessary for an understanding of electron diffraction, with specific information about our studies included later in the section. A second section is included in order to collect and summarize our results as well as to present information of a supplementary nature.

The details of the photoluminesence (PL) aspects of this work are presented in Chapter 4. The first section gives a basic description of the PL process in π—electron systems. Because the model we propose involves the interaction of the members of an excited dimer, a section is given to establishing a theoretical framework from which to study this interaction. Subsequent sections present the pertinent aspects of the luminescence data and reconcile the various aspects of the PL data to an excimer model. Parts of this chapter are devoted to explaining polycrystalline luminescence data in terms of modifications to the excimer picture.

In Chapter 5, the information presented in the earlier chapters is summarized, and possible extensions of this work are mentioned.

Chapter 2

Experimental

2.1 Growth Chambers, LEED and X-ray Analysis

The epitaxial growth of the samples took place in two separate UHV vacuum chambers. In the first chamber, the antimony surface was prepared by molecular beam epitaxy (MBE) on a substrate of nominally undoped p-type (111)A [18]. The growth was monitored in-situ through the use of reflection high-energy electron diffraction (RHEED). The Sb layer was grown by cooling the substrate to approximately 10 K below the nucleation temperature T_n in the presence of an Sb flux. After deposition of the Sb layer, the films were transferred in air to a second UHV chamber.

A schematic of this second UHV chamber, designed and built at Rice University, is given in Figure 2.1. The forty liter chamber is evacuated by five separate pumps, and has a base pressure below 5×10^{-11} torr. Initial rough evacuation is effected by means of a Leybold mechanical pump, which has the ability to pump down to 5×10^{-3} torr when exhausted to atmosphere. A Varian V200A 200 liter per second turbo molecular pump is used to pump the chamber into the high to ultra high vacuum regime.
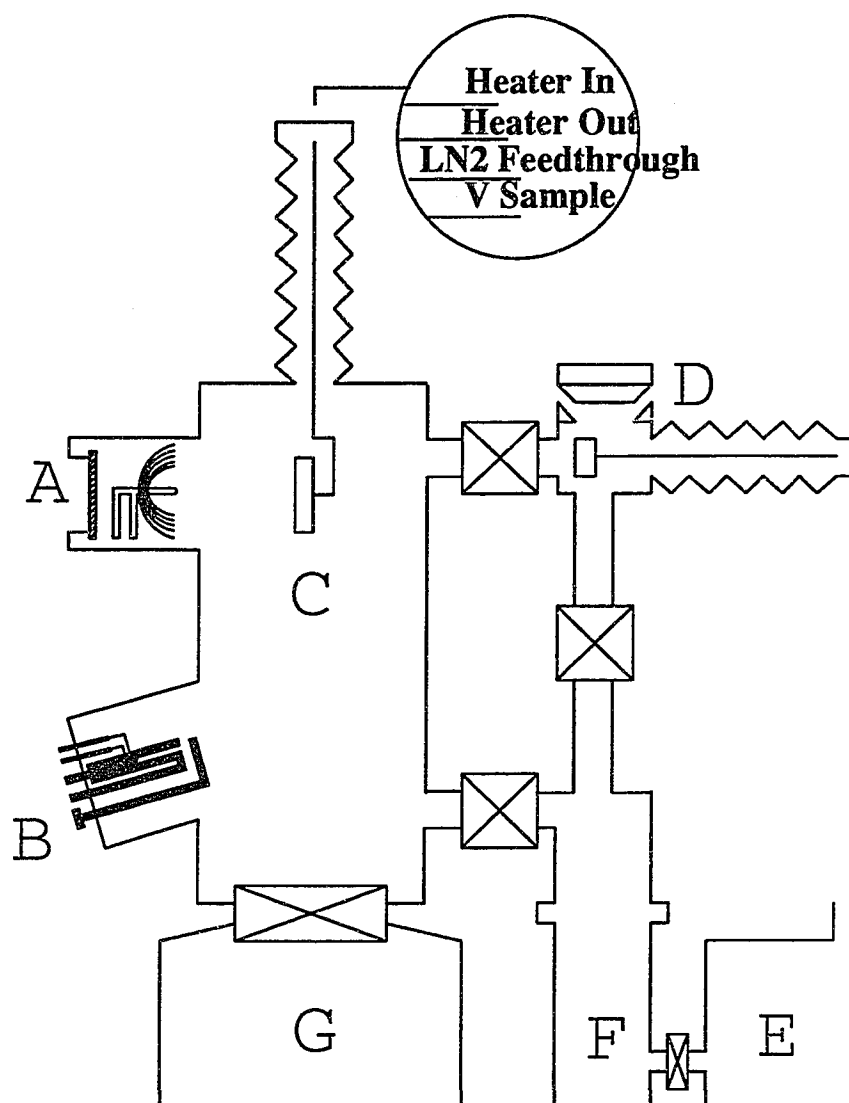
Figure 2.1: Schematic of Vacuum Chamber Used for Film Growth and LEED Analysis
A)LEED Apparatus and View Port, B)Effusion Cell, C)Sample Platen, D)Sample Introduction Chamber, E)Mechanical Pump, F)Turbo Pump, G)Ion Pump

At these pressures, a Varion Starcell Vacion Model 919-0105 230 liter per second ion pump is used to further decrease the pressure in the chamber. Ultimate base pressure is achieved through the use of a Varian Model 916-0017 filament type titanium sublimation pump in conjunction with a liquid nitrogen cryopump. Samples are loaded into and removed from the chamber by means of a load lock chamber. The load lock is evacuated by the roughing pump and the turbo molecular pump. The sample manipulator is a custom design supplied by Thermionics Northwest, Inc. It consists of an electrically isolated molybdenum sample platen on a stage that allows for 16 inches of translation along the vertical axis and one inch of translation along each horizontal axis. In addition, the sample platen is rotatable along both the chamber vertical axis and the sample normal axis. A tungsten heater is used to raise the sample temperature while a small liquid nitrogen dewar in thermal contact with the sample provides cooling capacity. The chamber contains an effusion cell for the deposition of C_{60}. The cell consists of a tantalum foil furnace supported on a high current feedthrough. The feedthrough leads are 0.635 cm copper rods. These are mated to the 304 series stainless steel supporting members of the furnace. The crucible itself is composed of graphite with a graphite aperture. A K-type thermocouple is inserted in the back of the graphite crucible, facilitating measurement of the temperature of the furnace.

The C_{60} deposition rate is measured using a quartz crystal micro-balance situated in close proximity to the sample. The micro-balance oscillation is tracked by a Maxtek, Inc. Model TM-100 quartz micro-balance monitor. A stylus profilometer was used to calibrate the quartz monitor. The chamber is also equipped for low-energy electron diffraction (LEED) experiments. The details of LEED as well as a schematic of the apparatus will be presented in separate section.

A disordered surface oxide forms on the Sb surface during transfer in air to the C_{60} deposition chamber, as indicated by a diffuse uniform LEED pattern. Because of this, the Sb films are first heated to 200°C for ten minutes prior to C_{60} deposition to desorb the surface oxide layer. At this point, a sharp LEED pattern is visible on the clean Sb layer. The C_{60} starting material was obtained using vapor phase purification [19], and was greater than 99.9% pure, as indicated by high performance liquid chromatography(HPLC). Sublimation of C_{60} took place with the graphite effusion cell held at approximately 400° C, with the chamber pressure at about 5×10^{-9} torr. The sample was held at $\sim 100^{\circ}$C during the growth. The deposition rate was approximately 0.4 Å/second, as measured by the quartz crystal microbalance.

LEED analysis of the C_{60} epilayer indicates epitaxial growth, and the absence of rotated domains. This is seen in the parallel orientation of the $[1\bar{1}0]$ direction for both

the Sb substrate and the C_{60} epilayer, despite the 16.1% mismatch between twice the Sb lattice spacing and the C_{60} lattice. For a more in depth LEED analysis see the Chapter 3.

X-ray diffraction measurements were taken *ex situ* using a sealed tube source. A Ge(220) monochromator, followed by a slit 66 cm away was used to select only the $K\alpha_1$ line. A radial $\theta - 2\theta$ scan indicated that the C_{60} film was entirely [111] oriented, with a cubic lattice parameter of 14.14 Å at 300 K. The transverse scan through the (111) C_{60} peak indicates a mosaic spread of 0.65^0 for the C_{60} film.

Immediately upon removal from the second chamber, the films were transferred in nitrogen to an inert atmosphere to be loaded into the optical sample chamber.

2.2 Apparatus For Luminescence Studies

The sample chamber used in these experiments is a closed system helium cryostat, model LTS-22-NGO-C-0.1, from RMC Technologies. The temperature was monitored by a four-lead silicon diode mounted on the second stage of the cold head, in close proximity to the sample. At equilibrium, the temperature given by the diode is accurate to within 1 K. Sample excitation was by means of a multi-line argon ion laser, with a line filter centered at 514.53 nm. The beam was focussed onto the sample with

a cylindrical lens to limit the intensity on the sample and to aid in the collection of the photoluminescence. Incident intensities were kept to less than 10 W/cm^2 to avoid polymerization of the C_{60} film. Raman spectra taken after prolonged irradiation showed that the Raman line originating from the $A_g(2)$ mode remained unshifted, indicating that the films were not polymerized [8]. A schematic of the equipment used to obtain photoluminescence and Raman spectra is given in Figure 2.2.

To collect the PL spectrum, the irradiated spot on the sample is imaged onto the 150 μm entrance slit of a double monochromator, consisting of two Jarrell-Ash 82-415 quarter meter monochromators in series. The exit slit is 100 μm. The monochromator resolution is about 0.6 meV. Absolute calibration was performed using the well characterized Raman spectrum of CCl_4, while relative calibration was achieved by using the spectral lines of a Hg lamp.
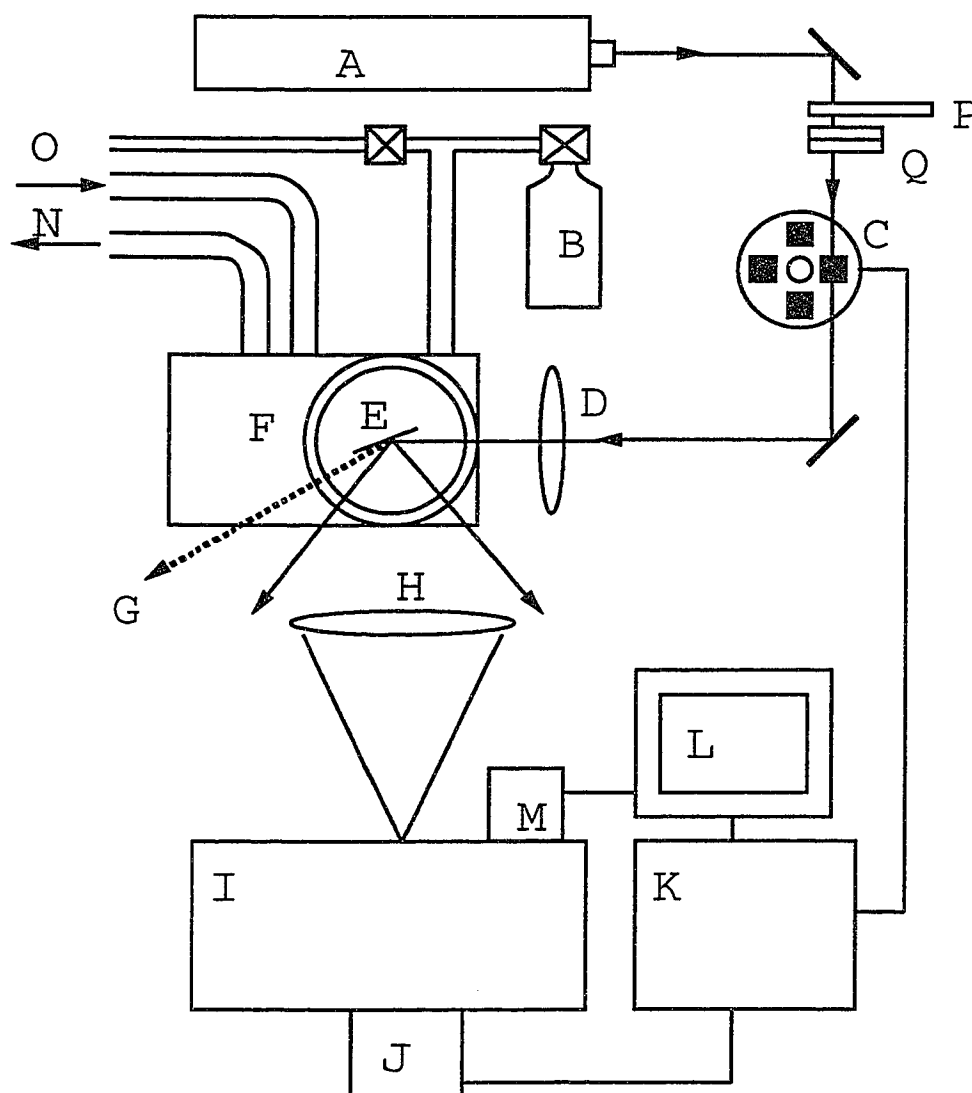
Figure 2.2: Experimental Apparatus For Observing PL and Raman Spectra
A)Multi-line Ar-Ion Laser, B)Sorption Pump, C)Chopper, D)Cylindrical Lens, E)Sample, F)Cryostat, G)Rayleigh Scattering, H)Collection Optic, I)Double Monochromator, J)Cooled PMT, K)Lock-In Amplifier, L)Personal Computer, M)Stepper Motor, N)Helium Supply and Return, O)Argon Backfill Line, P)Variable Attenuator, Q)Line Filter

Chapter 3

Low Energy Electron Diffraction (LEED)

3.1 Introduction

Low energy electron diffraction (LEED) came into widespread use as a surface analysis tool with the realization of affordable ultra high vacuum (UHV) technology. The information that LEED can provide ranges from detailed surface structure information to limited orientational and bulk structure information. In the energy range of our experiments (20 eV to 40 eV), the penetration depth of electrons into C_{60} is on the order of one monolayer [20]. (See Figure 3.1). For this reason we obtain primarily surface information, although a certain amount of insight can be gained by the observation of the substrate through partial layers of C_{60}. This will be explored briefly later in this section.

Although there are many uses for the type of information provided by LEED, we have been primarily concerned with the registry of overlayers with respect to the structure of a substrate surface; of particular interest is the registry of a C_{60} overlayer to the surface of an antimony substrate. Additionally, structural information derived
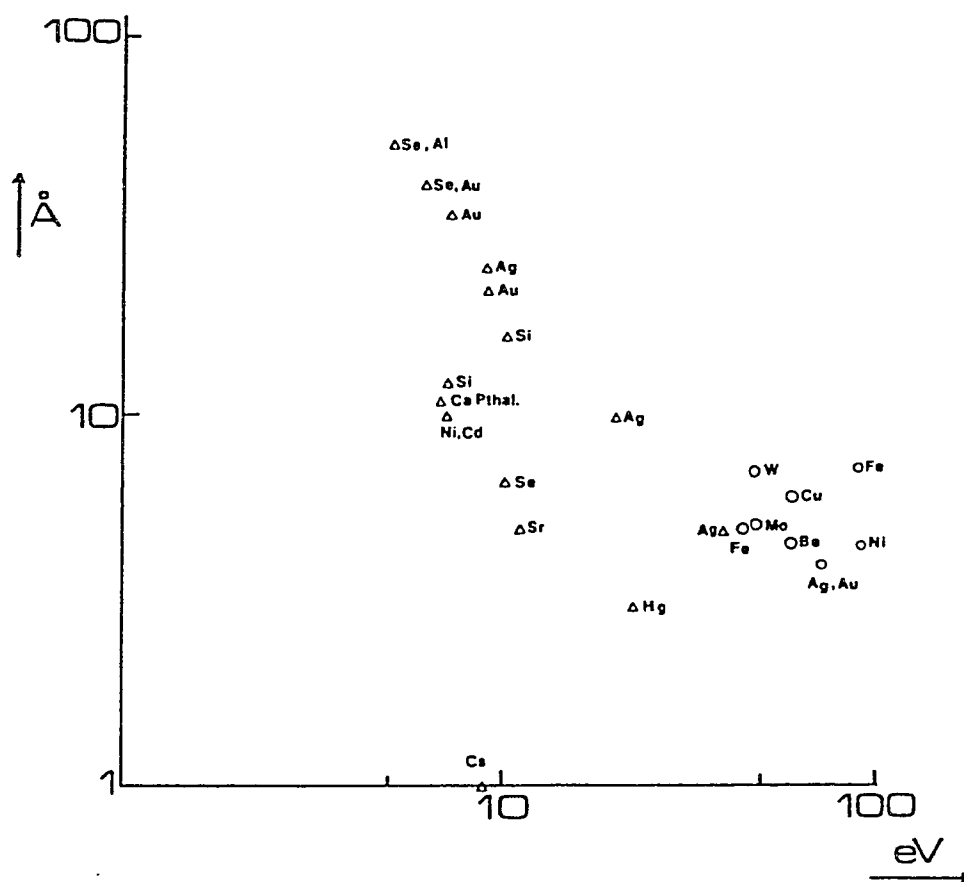
Figure 3.1: Electron Penetration Depth (or Escape Depth) as a Function of Electron Energy
after [20]

from LEED on the substrate can be used in conjunction with x-ray diffraction (XRD) studies [21] to calibrate measurements of the adlayer structural parameters [16].

Further reading on low-energy electron diffraction can be found in: *Low-Energy Electron Diffraction*, by M. A VanHove, W. H. Weinberg, and C. M. Chang [22]; *Electron Microscopy of Materials*, by Manfred Von Heimendahl [23]; and *Introduction to Solid State Physics*, by Charles Kittel [24].

3.2   LEED Background and Application

The LEED apparatus used in our experiments is a Princeton Research Instruments Reverse View LEED Optics, Model 8-120, used with Perkin-Elmer LEED Electronics, Model 11-020. A schematic of the optics is shown in Figure 3.2.

The optics is composed of four concentric hemispherical grids behind which is mounted a screen coated with phosphorescent material. The electron gun is situated behind the screen, emitting electrons through a hole in the screen and grids. The sample to be studied is placed at the center of curvature of the grids. If the sample is electrically isolated, it may be independently grounded so that beam current may be measured. The grid closest to the sample is generally grounded, to provide a field free region between the sample and the grid. The second and third grids are known as
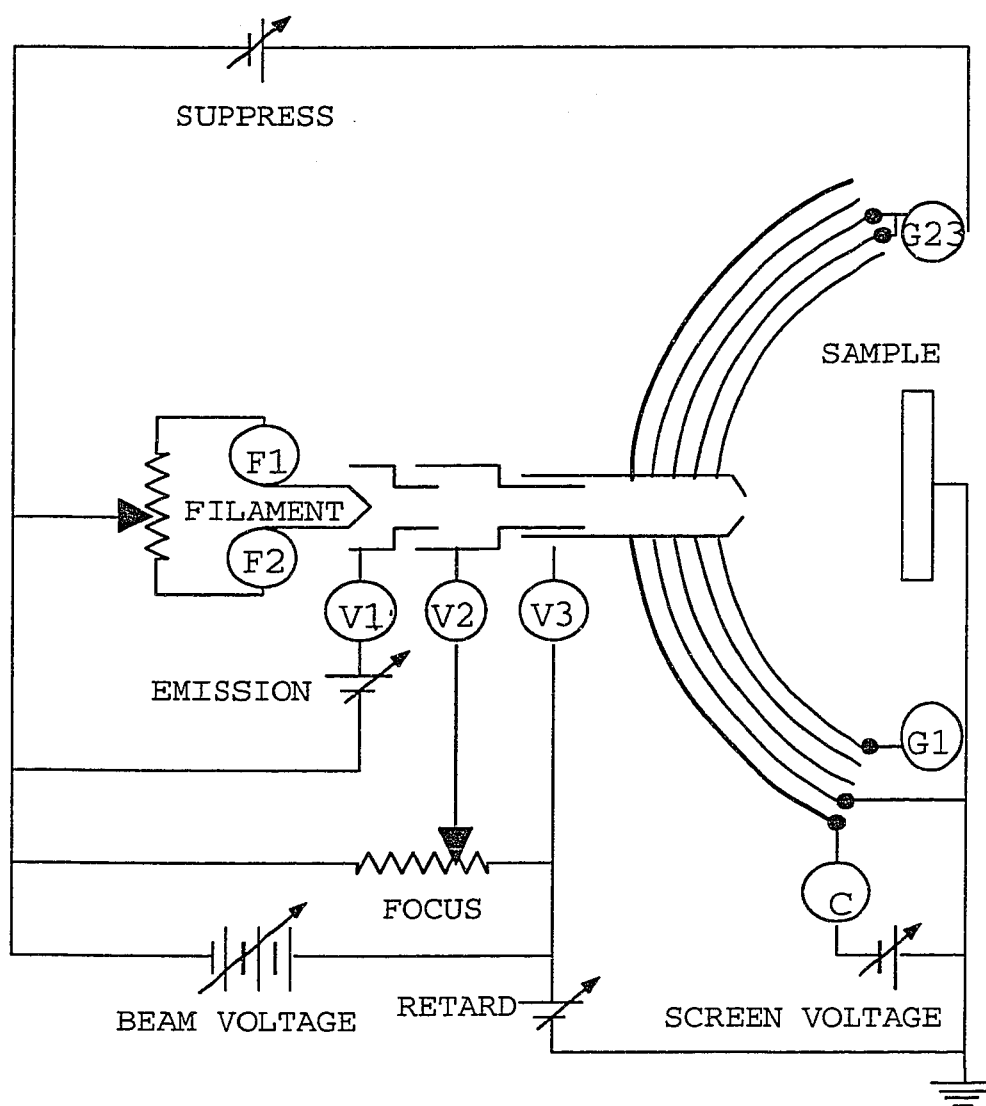
Figure 3.2: LEED Optics
Shown are viewport, electron gun, extraction and focussing sections, screen, and grids.

the suppressor grids. Since processes other than elastic diffraction take place as well, these grids are held at a voltage that will pass only elastically scattered electrons. The fourth grid is grounded. The collector screen is held at a high voltage to accelerate any electrons that have passed through the four grids. These accelerated electrons create the phosphorescence that is observed as the LEED pattern. This apparatus also has the ability to operate in the *retard* mode. In this mode a voltage is applied between the tip of the electron gun optics and ground. This has the effect of retarding the beam between the gun and the sample, and is crucial for minimizing space charge problems during very low energy measurements.

The formation of electron diffraction patterns is a direct consequence of the wave-like properties of moving particles. A particle having momentum p can be described as having a wavelength given by

$$\lambda = \frac{h}{p}. \tag{3.1}$$

The diffraction of electrons described by this relation can be interpreted in two different ways. One way to understand electron diffraction is in terms of Bragg scattering, using ideas not fundamentally different from those applied in x-ray diffraction (XRD). From another standpoint, because of the shallow penetration of low energy electrons into solids, diffraction could be viewed as the interference of waves scattering from an

array of point sources [22]. The formalisms used in a multilayer Bragg-type approach will be developed below [24]. This will be followed by simplifications to reconcile the theory to diffraction patterns observed for crystalline C_{60}.

The familiar Bragg law relates the incident angle, wavelength, and inter-planar spacing, d, as follows:

$$2d \sin \theta = n\lambda, \tag{3.2}$$

where n denotes the order of the diffraction. We are generally concerned with first order spots. This expression results from consideration of constructive interference between reflections from different planes, and thus relies upon the periodic nature of the solid in question. At this point it is important to make a distinction between the lattice and the basis. The lattice is an array of points having three dimensional periodicity, and is spanned by three *lattice vectors*. The basis is the unit of atoms or molecules that are located in the same orientation at every lattice point to create the physical crystal. Translation along any vector in the space of vectors spanned by the three defining lattice vectors will be a symmetry operation.

The electron density, $n(r)$, is periodic with the lattice. The exact electron density distribution within a unit cell is as important as the periodic distribution, and will

be explored later in this section. A lattice translation vector, $\mathbf{T}$, is defined as

$$\mathbf{T} = u_1\mathbf{a}_1 + u_2\mathbf{a}_2 + u_3\mathbf{a}_3 \qquad (3.3)$$

where $\mathbf{a}_i$ are the crystal axes. Using this, the electron density must obey

$$n(\mathbf{r} + \mathbf{T}) = n(\mathbf{r}). \qquad (3.4)$$

In one dimension, the periodic electron density can be expressed as the complex fourier expansion

$$n(x) = \sum_p n_p \exp i2\pi px/a \qquad (3.5)$$

where a is the period of the density function, $n(x)$. In three dimensions, we write the density function as

$$n(\mathbf{r}) = \sum_G n_G \exp(i\mathbf{G} \cdot \mathbf{r}). \qquad (3.6)$$

By (3.4) and (3.6), it must be true that

$$\exp(i\mathbf{G} \cdot \mathbf{r}) = \exp(i\mathbf{G} \cdot (\mathbf{r} + \mathbf{T})). \qquad (3.7)$$

This leads to the construction of the primitive reciprocal lattice vectors, $\mathbf{b}_i$, defined as

$$\mathbf{b}_1 = 2\pi\frac{\mathbf{a}_2 \times \mathbf{a}_3}{\mathbf{a}_1 \cdot \mathbf{a}_2 \times \mathbf{a}_3}; \quad \mathbf{b}_2 = 2\pi\frac{\mathbf{a}_3 \times \mathbf{a}_1}{\mathbf{a}_1 \cdot \mathbf{a}_2 \times \mathbf{a}_3}; \quad \mathbf{b}_3 = 2\pi\frac{\mathbf{a}_1 \times \mathbf{a}_2}{\mathbf{a}_1 \cdot \mathbf{a}_2 \times \mathbf{a}_3}. \qquad (3.8)$$

A reciprocal lattice vector $\mathbf{G}$ is given in terms of these primitive vectors as

$$\mathbf{G} = v_1 \mathbf{b}_1 + v_2 \mathbf{b}_2 + v_3 \mathbf{b}_3. \tag{3.9}$$

The vectors $\mathbf{b}_i$ are said to span reciprocal space. Thus for every real space lattice, there is an associated reciprocal space lattice, with a fixed spatial relation to the real lattice. For instance, the reciprocal space lattice for C_{60}, which has been found to have the face centered cubic (fcc) structure, is easily obtained using the formalism above. The fcc real space lattice vectors in rectangular coordinates are

$$\mathbf{a}_1 = \frac{1}{2}a(\mathbf{y} + \mathbf{z})$$

$$\mathbf{a}_2 = \frac{1}{2}a(\mathbf{x} + \mathbf{z})$$

$$\mathbf{a}_3 = \frac{1}{2}a(\mathbf{x} + \mathbf{y}).$$

Here, a is the cubic lattice parameter of the physical lattice. Entering these vectors into the expressions for the reciprocal lattice vectors, it can be shown that

$$\mathbf{b}_1 = (\frac{2\pi}{a})(-\mathbf{x} + \mathbf{y} + \mathbf{z})$$

$$\mathbf{b_2} = (\frac{2\pi}{a})(\mathbf{x} - \mathbf{y} + \mathbf{z})$$

$$\mathbf{b_3} = (\frac{2\pi}{a})(\mathbf{x} + \mathbf{y} - \mathbf{z}).$$

As depicted in Figure 3.3, the phase factor between two beams scattered at the origin and from some point r is $\exp[i(\mathbf{k} - \mathbf{k}') \cdot r] = \exp[i\Delta\mathbf{k} \cdot r]$. If we assume that the scattered intensity A is proportional to the local electron density in addition to
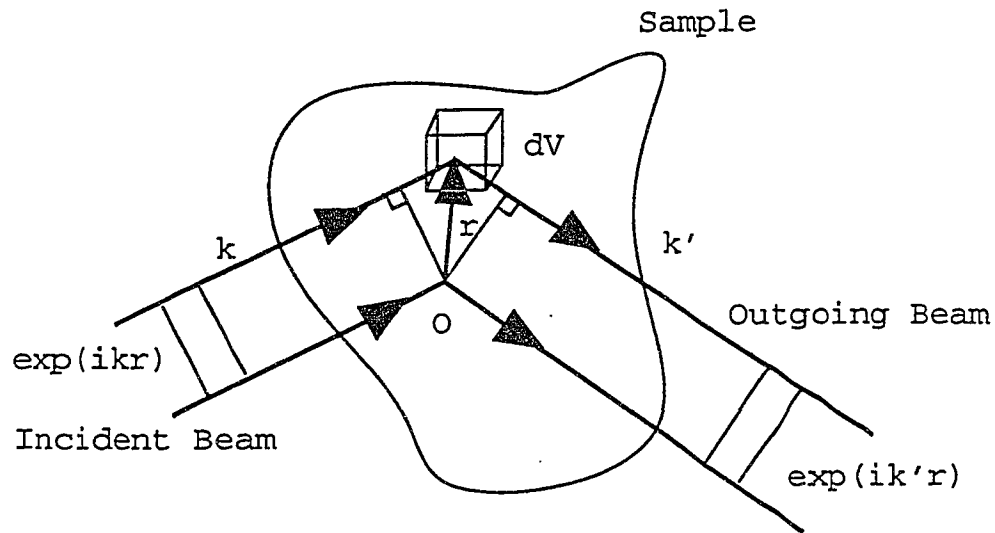
Figure 3.3: Scattering From Volume Element dV
The difference in phase angle relative to the incoming wave is (k-k′)·r. (After Kittel [24])

this phase factor, then

$$A \propto \int dV n(r) \exp(-i\Delta \mathbf{k} \cdot \mathbf{r}) \tag{3.10}$$

where the integral is over the volume. Using the expression for the electron density

postulated in (3.6), this can be written as

$$A \propto \sum_G \int dV n_G \exp[i(\mathbf{G} - \Delta \mathbf{k}) \cdot \mathbf{r}]. \tag{3.11}$$

This expression is maximum for values of $\Delta \mathbf{k}$ such that $\Delta \mathbf{k} = \mathbf{G}$. This is the fundamental condition for diffraction. The scalar product of $\Delta \mathbf{k}$ with $\mathbf{a}_1$ is

$$\mathbf{a}_1 \cdot \Delta \mathbf{k} = \mathbf{a}_1 \cdot \mathbf{G}. \tag{3.12}$$

Using (3.9), this can be expressed as

$$\mathbf{a}_1 \cdot \Delta \mathbf{k} = \mathbf{a}_1 \cdot (v_1 \mathbf{b}_1) = 2\pi v_1. \tag{3.13}$$

Taking similar scalar products using $\mathbf{a}_2$ and $\mathbf{a}_3$ we arrive at a set of equations known

as the Laue equations:

$$\mathbf{a}_1 \cdot \Delta \mathbf{k} = 2\pi v_1$$

$$\mathbf{a}_2 \cdot \Delta \mathbf{k} = 2\pi v_2$$

$$\mathbf{a}_3 \cdot \Delta \mathbf{k} = 2\pi v_3.$$

These are the geometrical embodiment of the diffraction condition (2). Each Laue

equation indicates that Δk must lie on a cone about that respective lattice vector.

The only way that this condition can be met is for three cones to intersect in a line

with Δk lying along the line of intersection.

Another way to visualize the condition for diffraction is the Ewald construction,

after P. P. Ewald [24], as shown in Figure 3.4. Recall that the condition for diffraction
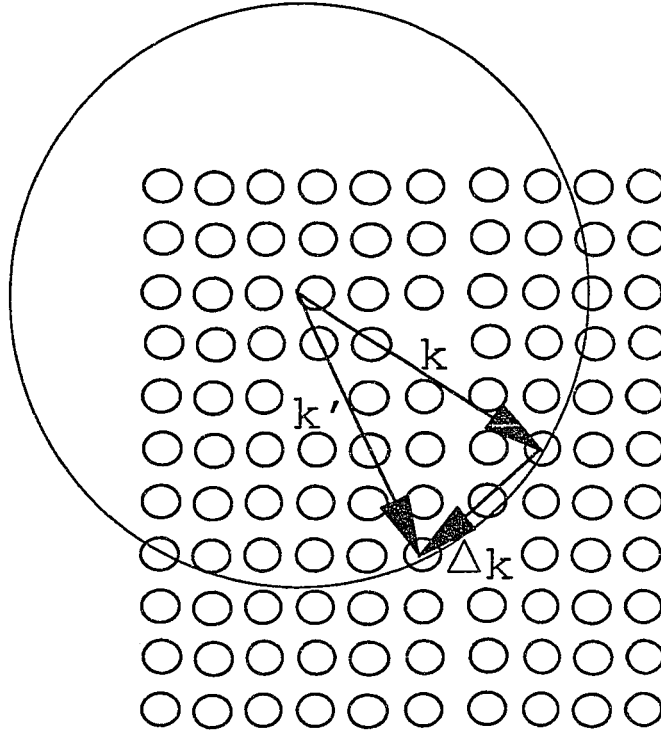
Figure 3.4: Ewald Construction
The tip of the incoming wave vector is envisioned to be at a point in reciprocal space.
A sphere at this radius will then pass through the other points in reciprocal space
that represent Bragg allowed reflections. Because both ends of the difference vector
lie on reciprocal lattice points, it is a reciprocal lattice vector, G, as required.

is simply that $k - k'$ must be equal to a reciprocal lattice vector. With this in mind, if the tip of the incoming wave vector is visualized to be at a point in reciprocal space, then any point at that radius that is also a point in reciprocal space will necessarily represent an allowed reflection. This method, as with the previous treatment, relies on elastic interaction of the electrons with the solid, i.e. the magnitudes of $\vec{k}$ and $\vec{k'}$ are equal. Further, knowledge of the structure factor, to be discussed below, is sometimes necessary in order to accurately predict the diffraction pattern. It can be seen in this construction that for large incoming wave vectors relative to b_i, the Ewald sphere essentially samples a flat cross section of reciprocal space. Thus, a LEED pattern can be seen to first approximation as a plane in reciprocal space.

This alone is not usually sufficient to determine expected diffraction patterns from a given material. While our treatment thus far has assumed sets of partially reflecting planes, the actual lattice contains discrete atoms or molecules at regular spacings in these planes. This means that in addition to effects from lattice periodicity, there are effects due to the basis structure that must be considered. It has been established that

$$A \propto \int dV n(\mathbf{r}) \exp(-i\Delta \mathbf{k} \cdot \mathbf{r}) \qquad (3.14)$$

which can be written as

$$A \propto \int dV n(\mathbf{r}) \exp(-i\mathbf{G} \cdot \mathbf{r}) \qquad (3.15)$$

when $\Delta \mathbf{k} = \mathbf{G}$. The scattering amplitude for the entire specimen can be written as

the sum over all N cells, which, since they are equivalent, appears as

$$F = N \int_{cell} dV n(\mathbf{r}) \exp(-i\mathbf{G} \cdot \mathbf{r}) = \mathbf{N}\mathbf{S_G}. \qquad (3.16)$$

F/N is often referred to as the structure factor, since it is characteristic of the structure

of the basis. The term $n(\mathbf{r})$ in (3.16) can be written as the sum of electron density

contributions from the various constituents of a cell at location r. Thus,

$$n(\mathbf{r}) = \sum_{j=1}^{s} n_j(\mathbf{r} - \mathbf{r}_j) \qquad (3.17)$$

where the sum is taken over all the elements of the cell. With this definition, the

structure factor may be rewritten as

$$S_{\mathbf{G}} = \sum_j \exp(-i\mathbf{G} \cdot \mathbf{r}_j) \int dV n_j(\mathbf{r} - \mathbf{r}_j) \exp(-i\mathbf{G} \cdot (\mathbf{r} - \mathbf{r}_j)). \qquad (3.18)$$

The integral in this expression will be a measure of the scattering capability of the

element in question, and will be a function solely of its properties. Without solving

it explicitly, we may group it into one atomic factor, generally labelled as the *atomic*

form factor, f_j. Thus the structure factor becomes simply

$$S_{\mathbf{G}} = \sum_j f_j \exp(-i\mathbf{G} \cdot \mathbf{r}_j). \qquad (3.19)$$

When taking this sum over identical atoms or molecules, as is generally the case, the atomic form factor may be extracted from the summation. Calculations of the structure factor for various lattices have led to what are commonly known as the *extinction laws* [23]. These laws dictate simply that certain diffractions allowed by the constraint $\Delta\mathbf{k} = \mathbf{G}$ may be absent from the diffraction pattern due to a structure factor extinction.

The structure factor for the fcc crystal structure is calculated as an example. The cubic cell of the fcc structure contains four identical atoms (molecules) at the coordinates 000, $0\frac{1}{2}\frac{1}{2}$, $\frac{1}{2}0\frac{1}{2}$, and $\frac{1}{2}\frac{1}{2}0$, referred to the cubic lattice parameter. These coordinates are put in to (3.19), resulting in

$$S_{\mathbf{G}} = f_j\{1 + exp[-i\pi(v_2 + v_3)] + exp[-i\pi(v_1 + v_3)] + exp[-i\pi(v_1 + v_2)]\}. \qquad (3.20)$$

Recall that v_i are the integral elements of the vector $\mathbf{G}$. Thus, $S_{\mathbf{G}}$ can be simplified to

$$S_{\mathbf{G}} = f_j[1 + (-1)^{(v_2+v_3)} + (-1)^{(v_1+v_3)} + (-1)^{(v_1+v_2)}]. \qquad (3.21)$$

From this it can be seen that if v_i are all odd, or if v_i are all even, $S_G = 4f_j$. Otherwise, if v_i are mixed, $S_G = 0$. Thus, we could expect to see in the LEED pattern only spots due to reciprocal lattice vectors of unmixed indices. Looking at Figure 3.5, it becomes clear that we actually see a complete cross section of the reciprocal lattice, with no spots absent.

This can be explained using a general plot of electron penetration depth vs. electron energy, Figure 3.1. For electron energies in the range from 0eV to 1500eV, electron penetration depths can be as low as one monolayer or as high as one thou-
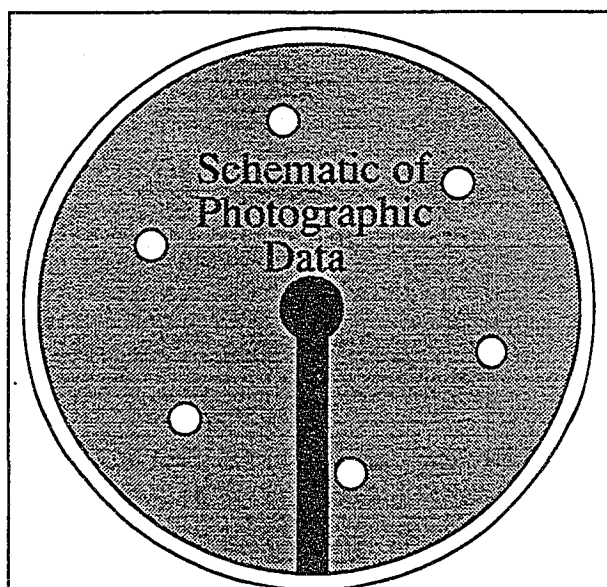
Figure 3.5: LEED on Several Monolayers of C_{60} Grown on Sb
LEED pattern does not change with increasing thickness.

sand monolayers. The minimum penetration occurs at around 30 eV. Our scans were taken using energies between 20 eV and 40 eV. The reason for using such low electron energies is that the C_{60} lattice has a very large (111) in-plane spacing. This causes the reciprocal lattice to be very compact compared to other materials. As will be discussed below, the radii of the LEED spots from the center spectral spot scale as the inverse of the incident electron energy. Thus, while LEED is performed at higher energies for most materials, the observed pattern for C_{60} is only distinguishable for relatively low electron energies. This being the case, the depths sampled in our LEED measurements probably do not extend past the first monolayer.

In recognition of this shallow penetration we modify the preceding formulation, which was based on the interference of reflections from stacked planes, to accomodate only surface reflections. The three dimensional lattice is replaced with a two dimensional surface net, and the Bragg conditions can be calculated for this new case. The two dimensional surface has a basis and a lattice, just like the three dimensional crystal. In terms of the Laue equations, the condition for diffraction from a single plane of particles can be viewed simply as the constraint that the change in momentum, Δk, must lie along the intersection of *two* cones [22]. This is a much simpler requirement than that of the 3-D case. Generally, no spots are disallowed on the basis of structure

factor extinctions for diffraction from a two dimensional array. Certainly, in the case at issue, the fcc (111) plane of C_{60}, there are no extinctions. The hexagonal surface net is spanned by two vectors of 10 Å length set at 60 degrees to one another, and the basis is composed of one molecule. The sum $\sum_j f_j exp(-iG \cdot r)$ becomes simply f_j.

The physical origin of diffraction spots from a surface is well explained using an array of scatterers to model the surface. The Huygens construction of the scattered intensity dictates that the spherical wave fronts emanating from the scatterers will merge into planar wave fronts in certain directions; these planar waves are the beams that propagate to the screen or detection device. An illustration of this principle is given in Figure 3.6.

The only substantive change in calculating diffraction patterns for a surface is to ignore the bulk structure factor in favor of the surface structure factor. For the sake of computation, it is equivalent to use the 3-D reciprocal lattice vectors, with the understanding that penetration is limited.

Experimentally, determining lattice distances in real space given LEED images is fairly straight forward. A diffraction spot at radius R on a screen at distance L from a sample being probed with electrons of wavelength λ will correspond to a spacing in
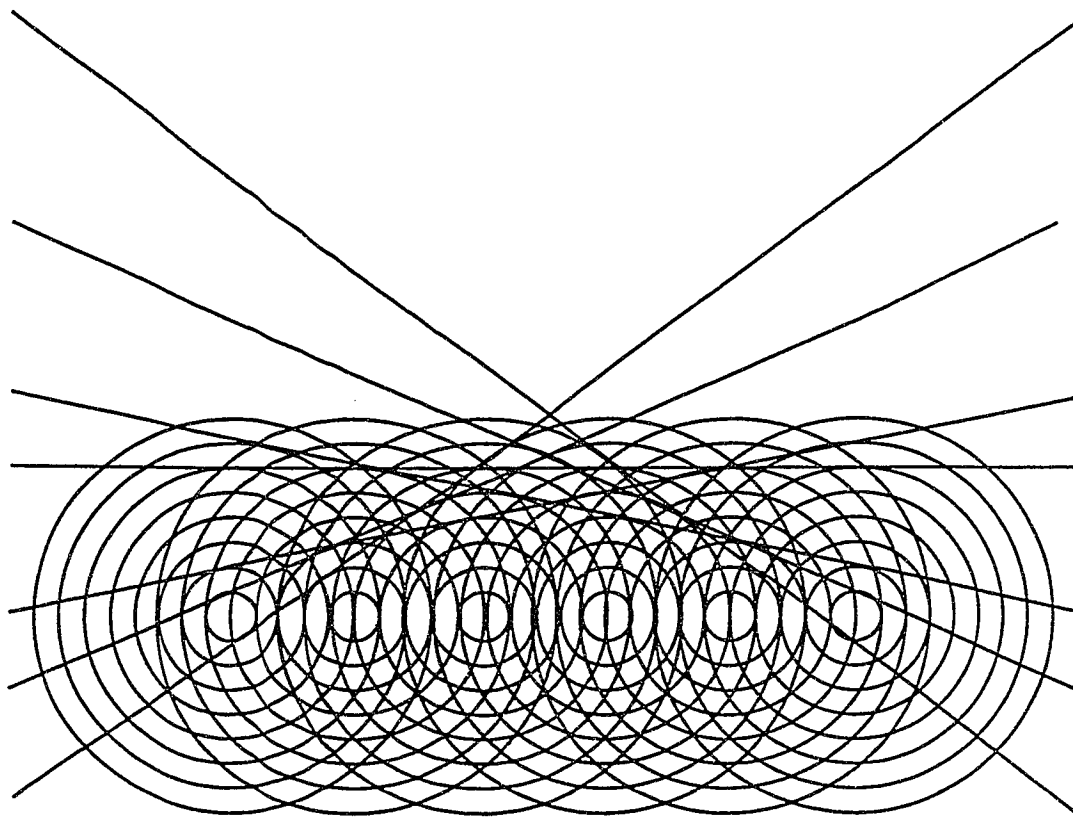
Figure 3.6: Illustration of Huygen's Principle
The spherical wavefronts from scatterers in a one dimensional array merge into planar wavefronts to form a diffraction pattern.

the sample of d in the following manner:

$$\lambda L = Rd \qquad (3.22)$$

This equation is found by manipulation of Bragg's law, (3.2). Traditionally, λL is called the *camera constant*, as it is the scaling factor between the reciprocal lattice and the diffraction pattern. The factor of 2π in (3.8) is a computational convenience and will now be neglected. Given this, the real lattice spacings and reciprocal spacings are simply inversely proportional; that is

$$g = \frac{1}{d}. \qquad (3.23)$$

Thus the relationship between the experimental parameters R, L, λ, and g is found from (3.22) to be

$$R = \lambda L g. \qquad (3.24)$$

While L is a distance that can be measured in the laboratory, it may change slightly as different samples are mounted to be studied. Thus it is desirable to have a method of calibration, so that for a given run, the camera constant may be easily ascertained. In our case, we have grown crystals on antimony, whose lattice parameters have been previously explored using XRD [21].
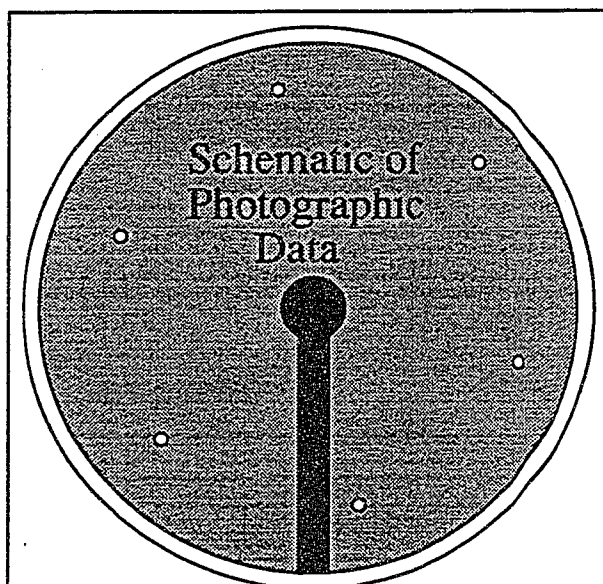
Figure 3.7: LEED on Thermally Cleaned (111) Sb Surface

Thus, the antimony (111) surface upon which we deposit C_{60} can be used for calibration of the camera constant. The LEED patterns shown in Figure 3.5 and Figure 3.7 were taken at the same energy and had the same sample to screen distance. Given the known in-plane spacing of the antimony (111) surface (4.308 Å), the pattern shown in Figure 3.7 gives a camera constant that is valid for Figure 3.5. Given this and the distance of the spots in Figure 3.7 from the center of the phosphorescent screen, the in-plane lattice spacing of the C_{60} (111) plane is found to be 10.2 ± 0.4 Å. This range includes the value of 10.02 Å commonly cited [25]. The sources of error

that have been considered in establishing the error bars on this measurement are the

radii of the diffraction spots from both surfaces.

Figure 3.5 can be used to imply that C_{60} grows on the antimony (111) surface

in a mode that preserves the symmetry directions of the substrate but that is vastly

lattice mismatched. This information can also be obtained from the pattern displayed

in Figure 3.8. The pattern displayed in this figure is from a partial monolayer of C_{60}

on antimony. This illustrates the way in which the patterns of the substrate and a

full or partial adlayer are superimposed. There are several points of interest to be
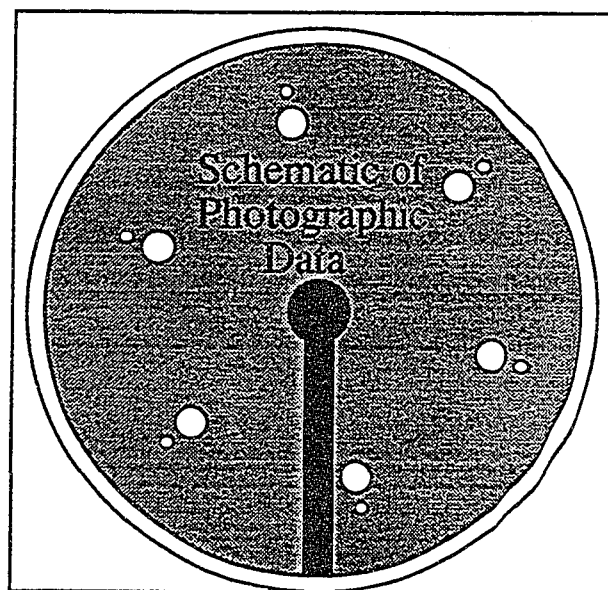
Figure 3.8: LEED Pattern of Submonolayer of C_{60} on Sb
Adlayer is not lattice matched, but preserves the symmetry and orientation of the substrate.

noted on this figure. Given the monolayer electron penetration at the energies used, this type of pattern can be used to verify monolayer coverages. Additionally, the fact that both the antimony and the C_{60} patterns were taken simultaneously allows for the possibility of better calibration of the camera constant.

3.3   Summary and Discussion

Low energy electron diffraction is used during the growth of highly crystalline thin film C_{60} for several reasons. It provides a method by which to ascertain the cleanliness of the intended substrate and then provides a continuous in-situ check of the crystallinity of the film during growth. In this capacity, it is used much as reflection high-energy electron diffraction (RHEED) is used in many molecular beam epitaxy (MBE) facilities. A secondary benefit of the use of LEED is the quantitative information it provides. We have used LEED to verify that the C_{60} surface lattice reflects a simple termination of the bulk, keeping the same lattice spacing and symmetry. Further, LEED has allowed us to determine that the growth mode of C_{60} on Sb is one in which the symmetry directions of the substrate are maintained in the adlayer despite a large lattice mismatch.

In concluding this discussion it should be mentioned that when C_{60} is cooled below 255K, the spinning movement of the molecules gives way to a ratcheting motion [17]. In this case the C_{60} molecule cannot be viewed as spherical. Differences in the frozen orientations of the moleculess cause the bulk lattice to take on simple cubic symmetry [26]. Since the molecular orientations are based on nearest neighbor interactions, it is unclear that the structure of the bulk termination will mimic that of the bulk. Preliminary LEED investigations indicate that while there is a change from the room temperature surface net upon cooling, this change seems to be the same as the change in the bulk, i.e. a transformation to a simple cubic structure. Comparison between our preliminary LEED data from cooled C_{60} and electron diffraction data presented by Tendeloo, et al., [11] indicates that the surface changes in the same way as the bulk.

Chapter 4

Photoluminescence (PL)

4.1 Introduction

Luminescence spectroscopy of organic molecular crystals can provide detailed information about the excited states of the molecules in a crystalline environment. Additionally, energy migration in crystals can be studied through the use of luminescence spectroscopy. Luminescence can be divided into fluorescence and phosphorescence. Fluorescence occurs during radiative deexcitation from the first excited singlet manifold to the ground state of the molecule or aggregation. Phosphorescence is the result of radiative deexcitation from the first excited triplet manifold. In addition to being categorized by the initial state, luminescence is also grouped by the particular excitation source. Thus there are: photoluminescence due to photon excitation; cathodoluminescence due to electron excitation; electroluminescence due to electrical excitation ; thermoluminescence due to thermal excitation, and so on. In general, the resulting luminescence depends only upon excitation energy, and is not affected by the particular means of excitation.

In organic molecules such as C_{60}, the luminescence phenomenon originates from the delocalized π–electrons. There is always an even number of electrons in a π–electron system [27], and thus the ground state of the system is always a singlet state. There are higher lying singlet states to which the system may be excited if the electrons do not undergo a spin flip during excitation. The ground singlet state and higher singlet states are denoted by S_0, S_1, S_2, etc. Triplet states also exist and are denoted T_1, T_2, etc. These are the resultant excited states when the electron undergoes a spin flip during excitation or deexcitation. Hund's rule requires that the
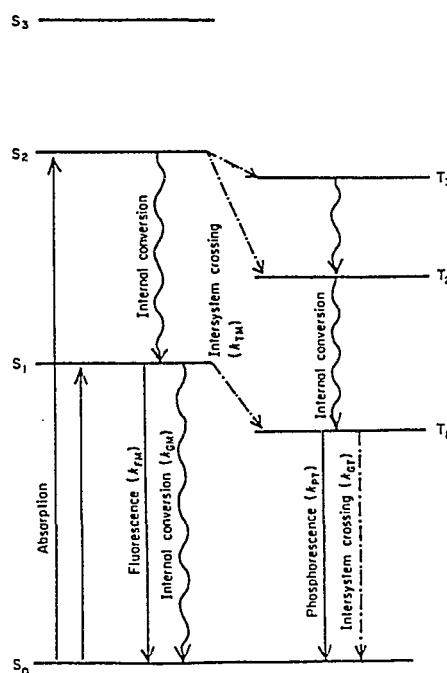
Figure 4.1: Energy Level Diagram for π–electron System from [27]

triplet states all lie below the corresponding singlet states. Thus T_1 is lower in energy than S_1, for instance. Figure 4.1 gives a schematic representation of the energy level system under discussion. Note that although the excitation source may be of sufficient energy to raise the system to higher lying excited states (S_n or T_n), the system will rapidly descend to the lowest excited state, due to internal conversion, or *thermalization*. These internal non-radiative transitions take place rapidly between the excited states above the first level, and are depicted in Figure 4.1. This is because internal conversion and intersystem crossing take place at rates that decrease with an increase in energy spacing between the states involved. Thus the luminescence observed is primarily due to radiative transitions from S_1 to S_0. The triplet T_1 state radiative decay to S_0 is very weak since quantum mechanical selection rules disallow the T_1 - S_0 transition. Due to this, absorption and radiative transitions between T_1 and S_0 take place at a much slower rate than the S_1 - S_0 transition. Furthermore, intersystem crossing takes place from the T_1 state to both the S_1 and S_0 states.

While radiative decay from the long lived T_1 state to S_0 will take place at some finite rate, there are other delayed radiative processes which take place from the S_1 singlet state to S_0. These delayed fluorescence processes are known as P-type and E-type delayed fluorescence. Both stem from the relatively long lifetime of the T_1 state.

If two molecules in the T_1 state collide, there is a probability that the result will be one molecule deexcited and one molecule left in S_1. In a solid, two molecules may not collide, but triplet excitons can interact to give the same effect. The radiative decay of this S_1 electron is known as P-type delayed fluorescence. This type of fluorescence may have energies greater than the excitation energy because each triplet exciton involved had at some point absorbed a pump photon. Alternatively, an electron in the T_1 state of a given molecule may be thermally excited with an energy on the order of $k_b T \simeq \Delta E(T_1 \Rightarrow S_1)$, causing a transition to S_1. This S_1 electron may undergo radiative deexcitation, resulting in E-type delayed fluorescence. Clearly, while occurring on the same time scale as the phosphorescence, delayed fluorescence will have the same spectral structure as ordinary fluorescence.

In order to more fully understand the information conveyed by luminescence it is important to keep in mind that each electronic level has vibrational structure superimposed on it. The process of photoluminescence can be envisioned to begin with a molecule in the ground vibrational level of the ground electronic state. Generally in molecular systems there are more than one vibrational level in each vibrational manifold, while in systems such as excimers there may be only one attractive ground state or, in fact, a repulsive ground state. The attractive ground state would be

due to van der Waals attraction while the repulsive ground state would be the result of Coulomb repulsion. In a system with at least one attractive ground vibrational state, an incident photon could excite the ground state electron up to some state S_n. Generally, electronic transitions occur so much more quickly ($\sim 10^{-15}$s) than the period of vibration ($\sim 10^{-12}$s) that the nuclei can be considered to be stationary during a transition. This is the Franck-Condon Principle. At this point, the system will be in a state of high potential energy. This energy will be rapidly converted to vibrational energy as the atomic nuclei adjust to accomodate the excited state of the electron. As this vibrational energy is lost to surrounding molecules the electron undergoes internal conversion and falls quickly to the lowest state in S_1, unless reexcitation occurs, as in the case of continuous wave pumping. The lifetime of the electron in the S_1 state depends on the rates of intersystem crossing, internal conversion, and radiative decay, and is generally on the order of a few nanoseconds. By Stokes' law, the radiation emitted during radiative decay from S_1 to S_0 will be at equal or longer wavelength than the excitation. This is easily understandable in that the excitation energy must be equal to or greater than the energy gap between S_0 and S_1, while the emitted wavelength corresponds just to the gap. Because decay almost always occurs from the bottom of the S_1 manifold and absorption almost always occurs from

the bottom of the S_0 manifold, the emission and absorption spectra will generally be mirror images of each other. When this is not the case, this indicates that there is not rapid or complete relaxation within the ground state or the excited state.

A further hindrance to straightforward interpretation of emission spectra is the formation of excimers. First observed in pyrene solution by Förster and Kasper in 1955, this phenomenon is known as *concentration quenching*. The fluorescence that these researchers observed from pyrene solutions seemed to be divided into two regions: highly structured emission observed at low concentrations; and broad, less structured emission that appeared at higher concentrations that seemed to quench the structured emission, as seen in Figure 4.2.

Because there was no corresponding change in the absorption spectra of the solutions, it became apparent that the source of the broad emission at high concentration was an excited state process. It was speculated that the process in question was the formation and decay of excimers, dimers which form only in the excited state. Thus the structured luminescence observed at low concentration could be attributed to monomer emission while the broad luminescence at higher concentrations could be seen as the decay of excimers. The featureless nature of the excimer emission was
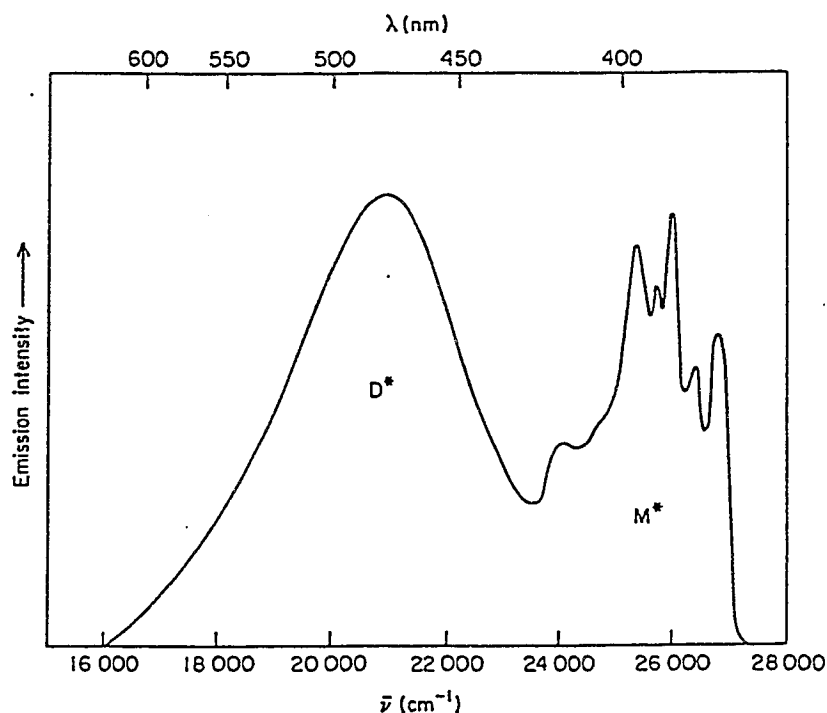
Figure 4.2: Luminescence Due to Concentration Quenching of Pyrene in Cyclohexane
After Lumb [27].

attributed to the fact that these excimers have a repulsive ground state. Thus, decay

from the S_1 state takes place down to a continuum state, not a narrow bound state.

Excimer formation is not at all uncommon. Many molecules, including pyrene,

benzene, napthalene, and certain forms of anthracene are known to form excimers.

Rare gas excimers have been observed, and the formation and decay of triplet excimers

in fullerenes in solution has been recently studied. Photoluminescence, sometimes

coupled with absorption spectroscopy, provides valuable insight into the details of

excimer formation and decay.

The model that best explains the observed PL spectrum of crystalline C_{60} involves the splitting of degenerate vibrational states within the S_1 level of the molecule caused by association with a second molecule, i.e. excimer splitting. The process begins with the absorption of a pump photon and ends with the emission of a photon due to fluorescence from some state in the S_1 manifold of the excimer to a single bound ground state:

$$h\nu_{pump} + C_{60} + C_{60} \Rightarrow C_{60}^* + C_{60} \Rightarrow [C_{60}C_{60}]^* \Rightarrow C_{60} + C_{60} + h\nu_{fluor.}. \qquad (4.1)$$
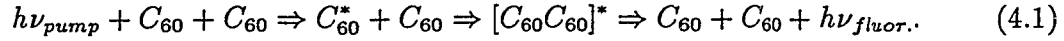
As mentioned above, $h\nu_{pump} \geq h\nu_{fluor.}$. The difference in energy is lost during thermalization to lower excited states. In order to explore how C_{60} luminescence fits this model, a theoretical framework for the vibronic interaction within an excited dimer is required.

4.2 Theoretical Background

In the adiabatic approximation, the vibronic wavefunctions (WF) are written as the product

$$\Psi(q,Q) = \phi(q,Q)\chi(Q) \qquad (4.2)$$

where q and Q are electronic and nuclear coordinates. Here ϕ(q,Q) is the electronic WF for the nuclei at rest, which is a solution of the electronic part of the Schrödinger

equation:

$$[H_q - W(Q)]\phi(q, Q) = 0 \tag{4.3}$$

Furthermore, $\chi(Q)$ is a solution to the Schrödinger equation for nuclear motion in the potential W(Q):

$$[T_Q + W(Q) - E]\chi(Q) = 0 \tag{4.4}$$

H_q is the electronic part of the Hamiltonian operator while T_Q is the operator representation of the kinetic energy of the nuclear skeleton of a single molecule.

Through algebraic manipulation of the previous two equations we arrive at:

$$[H_q + T_Q - E]\Psi(q, Q) = [T_Q\phi(q, Q) - \phi(q, Q)T_Q]\chi(Q). \tag{4.5}$$

This is a good approximation to the exact Schrödinger equation

$$[H_q + T_Q - E]\chi(q, Q) = 0 \tag{4.6}$$

if the term on the right hand side is relatively small. This condition is met if the electronically excited functions are well separated energetically for the nuclear configurations in question($\hbar\omega_{vibr} \ll E_{el}$).

4.2.1 Electronic Exchange Splitting in Excited Dimer

Using the facts that the electronic and nuclear motion are separable, and that the nuclear motion can be represented as a one dimensional oscillator, let us consider the electronic ground and excited states. If the ground and excited state vibrational modes are assumed to be harmonic oscillator eigenfunctions, then the Hamiltonians for nuclear motion in the ground and excited electronic states may be expressed as

$$H_N = T + \frac{1}{2}k_0(Q - \overline{Q}_0)^2 \qquad (4.7)$$

$$H_N' = T + \frac{1}{2}k(Q - \overline{Q})^2 \qquad (4.8)$$

respectively, where $T = -\frac{\hbar^2}{2M}\frac{d^2}{dQ^2}$ and k_0 and k are the force constants of the ground and excited electronic states. $\overline{Q}_0$ and $\overline{Q}$ are the equilibrium points of the ground and excited states respectively. The excited state Hamiltonian can be restated as

$$H_N' = H_N + C + AQ + BQ^2. \qquad (4.9)$$

Using (4.8) and equating coefficients of like terms,

$$A = k_0\overline{Q}_0 - k\overline{Q} \qquad (4.10)$$

$$B = \frac{1}{2}(k - k_0) \qquad (4.11)$$

$$C = \frac{1}{2}(k\overline{Q}^2 - k_0\overline{Q}_0^2). \qquad (4.12)$$

Thus, A represents a shift in the oscillator well, while B represents a distortion. If we assume that there is no distortion of the excited state well, i.e. $k = k_0$, then B= 0. In keeping with the shifted excited state indicated above, we represent the ground and excited potential wells for molecules a and b as

$$W_a = \frac{kQ_a^2}{2} \tag{4.13}$$

$$W_b = \frac{kQ_b^2}{2} \tag{4.14}$$

$$W_a' = E_0 + \frac{k(Q_a - c)^2}{2} \tag{4.15}$$

$$W_b' = E_0 + \frac{k(Q_b - c)^2}{2} \tag{4.16}$$

Where E_0 is the energy of electronic excitation and $c = \overline{Q} - \overline{Q}_0$. The binding energy of the exciton is

$$E_B = \frac{kc^2}{2}. \tag{4.17}$$

The molecular excited states of this system can be described as a local excitation of the a-molecule ($\phi_i' = \phi_a'\phi_b$) or the b-molecule ($\phi_i' = \phi_a\phi_b'$), where the excited state has energy

$$\langle \phi_i' | H_i | \phi_i' \rangle = E_e \tag{4.18}$$

In the limit where the intermolecular exchange integrals are small compared to the potential well depth, the excitonic states of the system are represented as linear

combinations of the locally excited configurations

$$\Phi_k = \sum_l^N c_{kl} \phi_l' \prod_{n \neq l}^N \phi_n. \tag{4.19}$$

For example, for a dimer we have

$$\Phi_1 = c_{1a} \phi_a' \phi_b + c_{1b} \phi_a \phi_b' \tag{4.20}$$

$$\Phi_2 = c_{2a} \phi_a' \phi_b + c_{2b} \phi_a \phi_b'. \tag{4.21}$$

The coefficients c_{kl} and energy values E_k can be obtained by the solution of the eigenvalue problem

$$\langle \phi_n | H_e | \phi_k \rangle = E_k \delta_{kn}. \tag{4.22}$$

In addition, the interaction matrix elements must be defined:

$$\langle \phi_m' \phi_n | V_{mn} | \phi_m \phi_n' \rangle = U_{mn} \tag{4.23}$$

where U_{mn} is an exchange integral between the configurations with m and n excited molecules. For the dimer,

$$U = \langle \phi_a' \phi_b | V | \phi_a \phi_b' \rangle \tag{4.24}$$

$$= \langle \phi_a \phi_b' | V | \phi_a' \phi_b \rangle. \tag{4.25}$$

Following the convention used by Förster [28], we write the dimer WF's as

$$\phi_+ = \cos \alpha \phi_a' \phi_b + \sin \alpha \phi_a \phi_b' \tag{4.26}$$

$$\phi_- = \sin \alpha \phi_a' \phi_b - \cos \alpha \phi_a \phi_b' \tag{4.26}$$

where the parameter α describes the degree to which the excitation is coupled from the excited molecule to the ground state molecule. As previously described, the ground state wave function for two molecules of the same kind is

$$\Phi_0 = \phi_a \phi_b \tag{4.27}$$

resulting in potential described in terms of the two nuclear coordinates

$$W_0 = \frac{\kappa}{2}(Q_a^2 + Q_b^2) \tag{4.28}$$

which is a paraboloid centered at $Q_a = Q_b = 0$. Using the electronic part of the Hamiltonian and the energies of excited molecules we can define

$$\langle \phi_a' \phi_b | H_a | \phi_a' \phi_b \rangle = W_{a'b} \tag{4.29}$$

$$\langle \phi_a \phi_b' | H_a | \phi_a \phi_b' \rangle = W_{ab'}. \tag{4.30}$$

where

$$W_{a'b} = (\kappa/2)[(Q_a - c)^2 + Q_b^2] + E_0 \tag{4.31}$$

$$W_{ab'} = (\kappa/2)[Q_a^2 + (Q_b - c)^2] + E_0.$$

Further we require that ϕ_+ and ϕ_- are orthogonal such that

$$\langle \phi_+ | H | \phi_- \rangle = 0. \tag{4.32}$$

Plugging Equations 4.26 into Equation 4.32 results in an expression which connects the parameter α to the splitting U:

$$\tan 2\alpha = \frac{2U}{W_{a'b} - W_{ab'}}. \tag{4.33}$$

In the weak coupling limit $2U \ll |W_{a'b} - W_{ab'}|$:

$$\alpha \sim 0 \quad \phi_+ = \phi'_a \phi_b \tag{4.34}$$

$$\phi_- = \phi_a \phi'_b \tag{4.35}$$

$$\alpha \sim \frac{\pi}{2} \quad \phi_+ = \phi_a \phi'_b \tag{4.36}$$

$$\phi_- = \phi'_a \phi_b \tag{4.37}$$

In the strong coupling limit, $2U \gg |W_{a'b} - W_{ab'}|$, with $\alpha \sim \frac{\pi}{4}$:

$$\phi_+ = \frac{1}{\sqrt{2}}(\phi'_a \phi_b + \phi_a \phi'_b) \tag{4.38}$$

$$\phi_- = \frac{1}{\sqrt{2}}(\phi'_a \phi_b - \phi_a \phi'_b) \tag{4.39}$$

where ϕ_+ is the symmetric case and ϕ_- is the antisymmetric case. Using these eigenfunctions to compute the diagonal elements of the electronic Hamiltonian yields

$$E_{\pm} = \frac{W_{a'b} + W_{ab'}}{2} \pm U. \tag{4.40}$$

Thus, in the strong coupling limit the energy of the symmetric and antisymmetric cases differ by 2U, which is known as the *exciton splitting*.

In order to evaluate a case that is neither of the above mentioned extremes, the α—parameterized wavefunctions are used to compute the energy eigenvalues:

$$E_{\pm} = \frac{W_{a'b} \pm W_{ab'}}{2} \pm \frac{U}{\sin 2\alpha}. \tag{4.41}$$

By noting that

$$\tan 2\alpha = \frac{2U}{W_{a'b} - W_{ab'}} = \frac{2U}{\frac{\kappa}{2}((Q_a - C)^2 + Q_b^2) - \frac{\kappa}{2}((Q_b - C)^2 + Q_a^2)} \tag{4.42}$$

we arrive at

$$W_{\pm} = E_0 + \frac{\kappa}{2}(Q_1^2 + Q_2^2 + c(Q_1 + Q_2)) \pm \frac{1}{2}\sqrt{\kappa^2 c^2(Q_1 - Q_2)^2 + 2U^2}. \tag{4.43}$$

For $|U| \geq \frac{\kappa c^2}{2}$ we have two parabolic surfaces of revolution in the 3-D space (Q_a, Q_b, E) with minima at $Q_a = Q_b = \frac{c}{2}$. For $|U| < \frac{\kappa c^2}{2}$ there is a minimum at $Q_a = Q_b = \frac{c}{2}$, with the minima for the W_- surface at

$$Q_a = \frac{c}{2} \pm \frac{1}{2}\sqrt{c^2 - \frac{4U^2}{\kappa^2 c^2}} \tag{4.44}$$

$$Q_b = \frac{c}{2} \mp \frac{1}{2}\sqrt{c^2 - \frac{4U^2}{\kappa^2 c^2}} \tag{4.45}$$

As the most important details lie in the perpendicular plane through $Q_a = Q_b = c$

we use the following coordinate transformation

$$x = \frac{1}{\sqrt{2}}(Q_a - Q_b)$$

$$y = \frac{1}{\sqrt{2}}(Q_a + Q_b) - \frac{c}{\sqrt{2}}$$

to arrive at an expression for the potential curves:

$$W_\pm = E_0 + \frac{\kappa c^2}{4} + \frac{\kappa}{2}(x^2 + y^2) \pm \sqrt{U^2 + \frac{\kappa^2 c^2 x^2}{2}} \qquad (4.46)$$
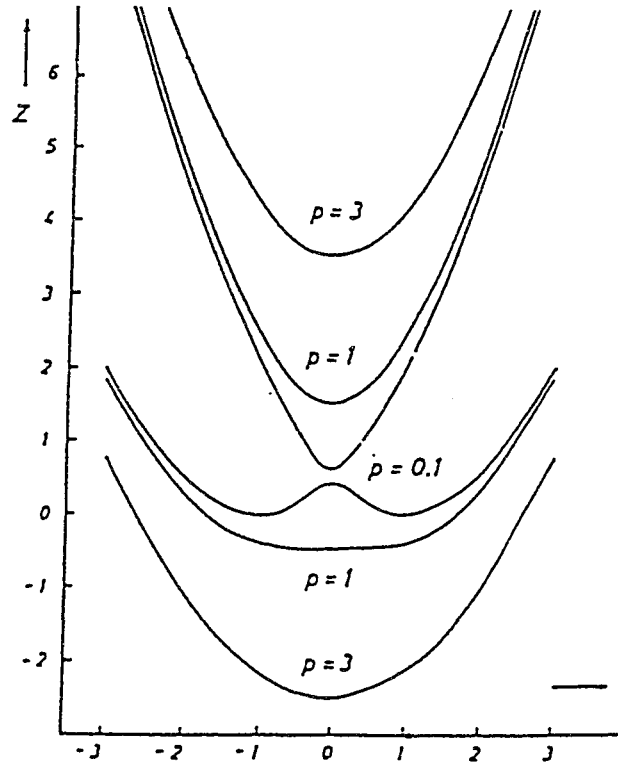
Figure 4.3: Potential Surfaces in Transformed Coordinates as a Function of p

from Förster [28]

This expression can be simplified using the coupling parameter $p = (2|U|)/(\kappa c^2)$.

For $p \geq 1$(strong coupling), there is a minimum at $x = y = 0$, as shown in Figure 4.3.

For $p < 1$ (weak coupling), there are minima at

$$x = 0, y = 0 \quad W_{+(min)} = E_0 + \frac{\kappa c^2}{4} + |U| \tag{4.47}$$

$$x = \pm\sqrt{\frac{1-p^2}{2}}, y = 0 \quad W_{-(min)} = E_0 - \frac{U^2}{\kappa c^2}. \tag{4.48}$$

The exciton splitting is

$$W_{+(min)} - W_{-(min)} = 2U \qquad\qquad p \geq 1 \tag{4.49}$$

$$W_{+(min)} - W_{-(min)} = |U| + \frac{\kappa c^2}{4} - \frac{U^2}{\kappa c^2} \qquad p < 1$$

The splitting in the emitted photon energy, E_{ph}, is given by

$$E_{ph\pm} = W_{\pm,min} - W_0. \tag{4.50}$$

Using (4.46) we can describe the ground state in transformed coordinates as

$$W_0 = \frac{\kappa x^2}{2} + \frac{\kappa}{2}(y + \frac{c}{\sqrt{2}})^2 \tag{4.51}$$

which yields

$$E_{ph+} = E_0 + |U| \tag{4.52}$$

$$E_{ph-} = E_0 - \frac{\kappa c^2}{2} \quad \text{for} \quad p \leq 1$$

$$= E_0 - |U| \quad \text{for} \quad p \geq 1.$$

This indicates a splitting of

$$\Delta E_{ph} = E_{ph+} - E_{ph-} = \frac{\kappa c^2}{2} + |U| \quad \text{for} \ |U| \leq \frac{\kappa c^2}{2} \tag{4.53}$$

$$= 2|U| \qquad\qquad \text{for} \ |U| \geq \frac{\kappa c^2}{2}. \tag{4.54}$$

4.2.2 Electron-Vibration Interaction Splitting in the Weakly Coupled Excited Dimer

In order to include vibrational effects in the splitting calculations, we write the ground state WF, in the weak coupling scheme, as

$$\Psi_{o,uw} = \phi_a \phi_b \chi_{ua} \chi_{wb} \tag{4.55}$$

where χ_{ua} and χ_{wb} are the eigenfunctions of the vibrational hamiltonians. If we take the energy of the electronic ground state to be zero,

$$E_{o,uw} = \langle \Psi_{o,uw} | H | \Psi_{o,uw} \rangle = (u + \frac{1}{2})\hbar\omega_0 + (w + \frac{1}{2})\hbar\omega_0 = (u + w + 1)\hbar\omega_0 \tag{4.56}$$

In this harmonic approximation, these vibronic states are (v+w+1)-fold degenerate (ground state). In the weak coupling approximation, electronic excitation is concentrated on one molecule ($\phi_a'\phi_b$-wavefunction) or the other ($\phi_a\phi_b'$). This situation is described by $\alpha \simeq 0$ or $\alpha \simeq \frac{\pi}{2}$ and by potential surface W, plotted in Figure 4.3

for p=0.1. This potential surface illustrates that vibrations occur in the basin of attraction for the first molecule($Q_a = c$, $Q_b = 0$) if it is excited, or for the second molecule($Q_a = 0$, $Q_b = c$). Therefore we must write the oscillator WF χ'_{ua} (prime denotes excited state potential well) for u-vibrational level if the a-molecule is excited. Thus for sufficiently low vibronic states we can write

$$\Psi_{\pm uw} = \frac{1}{\sqrt{2}}[\phi'_a \phi_b \chi'_{ua} \chi_{wb} \pm \phi_a \phi'_b \chi_{wa} \chi'_{ub}] \qquad (4.57)$$

Energies of the states must be calculated as the diagonal elements of the Hamiltonian.

$$H = H_{el.vib.} + V \qquad (4.58)$$

$$E_{\pm uw} = \langle \Psi_{\pm uw}|H_{el.vib.} + V|\Psi_{\pm uw}\rangle =$$

$$\frac{1}{2}\{\langle \phi'_a \chi'_{ua} \phi_b \chi_{wb}|H_{el.vib}|\phi'_a \chi'_{ua} \phi_b \chi_{wb}\rangle +$$

$$\langle \phi_a \chi_{wa} \phi'_b \chi'_{ub}|H_{el.vib}|\phi_a \chi_{wa} \phi'_b \chi'_{ub}\rangle \pm$$

$$\langle \phi'_a \phi_b|V|\phi_a \phi'_b\rangle\langle \chi'_{ua}|\chi_{wa}\rangle\langle \chi_{wb}|\chi'_{ub}\rangle \pm$$

$$\langle \phi_a \phi'_b|V|\phi'_a \phi_b\rangle\langle \chi_{wa}|\chi'_{ua}\rangle\langle \chi'_{ub}|\chi_{wb}\rangle\} =$$

$$\frac{1}{2}\{E_0 + (u + \tfrac{1}{2})\hbar\omega' + (w + \tfrac{1}{2})\hbar\omega_0 +$$

$$E_0 + (w + \tfrac{1}{2})\hbar\omega_0 + (u + \tfrac{1}{2})\hbar\omega' \pm$$

$$U S_{uw} S_{uw}\}$$

$$E_{\pm uw} = E_0 + (u + \frac{1}{2})\hbar\omega' + (w + \frac{1}{2})\hbar\omega_0 \pm U S_{uw}^2 \tag{4.59}$$

For vibrational overlap integrals (Frank-Condon integrals) we use the accepted designation for i−th molecule:

$$\langle \chi_{ui} | \chi'_{wi} \rangle = \langle \chi'_{wi} | \chi_{ui} \rangle = S_{uw} \tag{4.60}$$

$S_{uw} \neq 0$ because both vibrational functions belong to different centers. $S_{uw} < 1$ due to completeness relation $\sum_u S_{uw}^2 = \sum_w S_{uw}^2 = 1$. Therefore, the splitting in 4.54 is reduced by a factor of S_{uw}^2. For the lower vibrational states:

$$S_{00} = e^{-\frac{\gamma}{2}} \sqrt{\frac{2\sqrt{\omega_0 \omega'}}{\omega_0 + \omega'}} \tag{4.61}$$

$$S_{01} = \sqrt{\gamma} e^{-\frac{\gamma}{2}} \sqrt{\frac{2\omega'}{\omega_0 + \omega'}} \tag{4.62}$$

$$S_{10} = -\sqrt{\gamma} e^{-\frac{\gamma}{2}} \sqrt{\frac{2\omega_0}{\omega_0 + \omega'}}. \tag{4.63}$$

For the case of degenerate weak coupling, $\omega_0 = \omega'$. In this case (4.59) is valid only for u=w=0 (0-0 transitions).

$$E_{\pm 00} = E_0 + \hbar\omega_0 \pm U e^{-\gamma} \tag{4.64}$$

$$\gamma = \frac{kc^2}{2\hbar\omega_0} \, , \, \frac{kc^2}{2} \equiv E_b \tag{4.65}$$

For higher vibronic levels in the case of degenerate weak coupling, we must take symmetric and antisymmetric vibrational WF's for an excited a molecule (the sign in

the parentheses, second sign in Ψ subscript) and overall symmetric and antisymmetric

vibronic WF (constructed by interchanging a and b for the second term, with $\pm$ sign

in brackets, first sign in Ψ subscript):

$$\Psi_{1\pm\pm} = \frac{1}{2}[\phi'_a\phi_b(\chi'_{1a}\chi_{0b} \pm \chi'_{0a}\chi_{1b}) \pm \phi'_b\phi_a(\chi'_{1b}\chi_{0a} \pm \chi'_{0b}\chi_{1a})]. \tag{4.66}$$

The signs in parentheses are interchanged independently from the signs outside (in

brackets). Therefore, the total number of states is 4. Their energies are calculated as

diagonal elements of the Hamiltonian:

$$E_{1+\pm} = \langle\Psi_{1+\pm}|H|\Psi_{1+\pm}\rangle \tag{4.67}$$

$$= \frac{1}{4}\{2E_0 + 2(1 + \frac{1}{2})\hbar\omega_0 + 2E_0 + 2(0 + \frac{1}{2})\hbar\omega_0 + \tag{4.68}$$

$$U(S_{01}S_{01} + S_{10}S_{10} \pm S_{11}S_{00} \pm S_{11}S_{00} + S_{01}S_{01} \tag{4.69}$$

$$+S_{10}S_{10} \pm S_{00}S_{11} \pm S_{11}S_{00})\} \tag{4.70}$$

$$= E_0 + 2\hbar\omega_0 + U(S_{01}^2 \pm S_{00}S_{11}). \tag{4.71}$$

In the same manner

$$E_{1-\pm} = E_0 + 2\hbar\omega_0 + U(S_{01}^2 \pm S_{00}S_{11}). \tag{4.72}$$

Here we used eigenvalues of the single molecular Hamiltonian ($U = 0$), the non-diagonal interaction term

$$\langle \phi'_a \phi_b | V | \phi_a \phi'_b \rangle = U \tag{4.73}$$

and the Franck-Condon overlap factors for $\omega' = \omega_0$:

$$\langle \chi_{0a} | \chi'_{1a} \rangle = \langle \chi'_{1a} | \chi_{0a} \rangle \equiv S_{01} = \sqrt{\gamma} e^{-\frac{\gamma}{2}} \tag{4.74}$$

$$\langle \chi'_{0a} | \chi_{1a} \rangle = \langle \chi'_{1a} | \chi_{0a} \rangle \equiv S_{10} = -\sqrt{\gamma} e^{-\frac{\gamma}{2}} \tag{4.75}$$

$$\langle \chi_{0a} | \chi'_{0a} \rangle = S_{00} = e^{-\frac{\gamma}{2}} \tag{4.76}$$

$$\langle \chi_{1a} | \chi'_{1a} \rangle = S_{11} = (1 - \gamma) e^{-\frac{\gamma}{2}}. \tag{4.77}$$

Using this we have

$$S_{01}^2 + S_{00} S_{11} = e^{-\gamma}[\gamma + (1 - \gamma)] = e^{-\gamma} \tag{4.78}$$

$$S_{01}^2 - S_{00} S_{11} = e^{-\gamma}[\gamma - (1 - \gamma)] = -e^{-\gamma}(1 - 2\gamma)$$

So we obtain from (4.71) and (4.72)

$$E_{1++} = E_0 + 2\hbar\omega_0 + U e^{-\gamma} \tag{4.79}$$

$$E_{1+-} = E_0 + 2\hbar\omega_0 - U e^{-\gamma}(1 - 2\gamma)$$

$$E_{1--} = E_0 + 2\hbar\omega_0 + U e^{-\gamma}(1 - 2\gamma)$$

$$E_{1-+} = E_0 + 2\hbar\omega_0 - U e^{-\gamma}$$

In examining (4.79) it is clear that $E_{1\pm} - E_{1-+} = E_{+00} - E_{-00}$. Figure 4.4, taken from

[29] shows the change of the energy levels splitting, versus γ, which characterizes the

exciton binding energy as $\gamma = \frac{kc^2}{2(\hbar\omega_0)}$.

4.3 Theory of C_{60} PL at Low Temperatures

4.3.1 Single Crystal Thin Film C_{60}

The molecules in crystalline C_{60} are held together by weak van der Waals forces,

which affect the electronic states of each molecule only slightly. Thus, while the
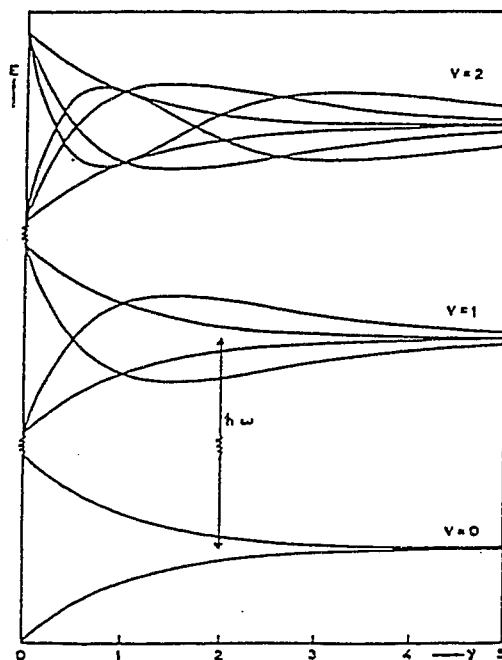

Figure 4.4: Splitting in the Weak-Coupling Scheme as a Function of
Electron-Vibration Interaction
from Siebrand, Journ. Chem. Phys., 1964 [29]

properties of the ground state are essentially additive, those of the excited states are not. In excited electronic states the intermolecular coupling is enhanced relative to the ground state via electronic exchange, as discussed in the previous section for the general case. This enhanced excited-state coupling, which often results in the appearance of excited state complexes (exciplexes), has been widely discussed in the context of the spectroscopy of molecular crystals [30, 31, 32, 33, 29]. For a single C_{60} molecule, the first electronic dipole transition (h_u-t_{1u}) is forbidden and, therefore, luminescence occurs due to vibronic mixing with the higher lying orbitals [13]. This is manifested as an inhibition of the 0-0 transition between the ground vibrational states and an enhancement of the 1-0 transition from the vibrationally excited state. In an effort to understand the flourescence of high purity single crystal C_{60} thin films, we consider it in the framework of a complex of two C_{60} molecules. Interaction of the molecules can be expected due to the close packed structure of C_{60}, and is strongly suggested by the observation of orientational clusters even in the ground state [34]. The separation between the centers of the nearest neighbor C_{60} molecules in the usual face centered cubic (fcc) structure is about 10.02 Å while the diameter of each molecule is 10.18 Å, with the inclusion of the outlying π orbitals [13]. The C_{60} molecules, like the constituents of rare gas crystals, are held apart by

the repulsive interaction of neighbors with filled valence shells. Electronic excitation of a C_{60} molecule, or a rare gas atom, relieves the closed shell condition, opening the possibility of covalent bonding. It can be seen from this that the interaction between carbon atoms from adjacent molecules may be significant, particularly for temperatures less than 90 K where rotational motion of the balls ceases. Indeed, Raman and resonance-Raman spectroscopy studies indicate that discernable crystal field effects do occur in solid state C_{60} [1, 35]. Also indicative of significant solid state interaction is the phase transition at T= 255K, which has been shown by NMR to be the onset of rotational ordering of the molecules. Theoretical investigations have used atom-atom potentials between atoms of adjacent molecules in conjunction with an interacting bond model to reproduce the phase transition at 255K with reasonable accuracy [36]. This would seem to indicate that there are distinct intermolecular interactions, particularly affecting the regions in closest contact. In a close packed structure, six basis units surround a molecule in the (111) plane, added to three from the embedding plane and three from the covering plane. Thus it would seem possible that an excitation can be spread over and affect a group of up to thirteen molecules in solid C_{60}. Investigations of the potential surfaces for molecular complexes ranging from 2 to 10 molecules with the electronic Hamiltonian including the nondiagonal

bimolecular electronic interaction term U show that all the essential features of the potential surfaces (minima values and their dependences on U) already appear in the bimolecular complex. Therefore it is justified to concentrate on the C_{60} dimer with the inclusion of vibrations to gain an understanding of the PL spectrum of solid C_{60}. In solid C_{60}, it is reasonable to assume that vibronic mixing would play a role in the luminescence spectrum for the case of weak intermolecular coupling between the electronically excited state of one C_{60} molecule and a ground state nearest neighbor. Due to the structure of the C_{60} crystal, an excited molecule can be expected to interact with the molecules closest to it.

The photoluminescence spectrum of single crystal C_{60} taken at 10 K is shown in Figure 4.5.

The experimentally obtained quantum efficiency was $\sim 5 \times 10^{-4}$, consistent with other published reports [37, 38]. Four well-resolved peaks are observed at the high energy side of this spectrum, at 1.767, 1.735, 1.696, and 1.664 eV, respectively, accompanied by a broad shoulder that can be resolved into two peaks located at 1.627 and 1.524 eV. The individual peaks are somewhat broader in these single crystal thin films than what have been reported for free-standing crystallites, however we do not observe significant sample-to-sample variation in our single crystal thin film photolu-
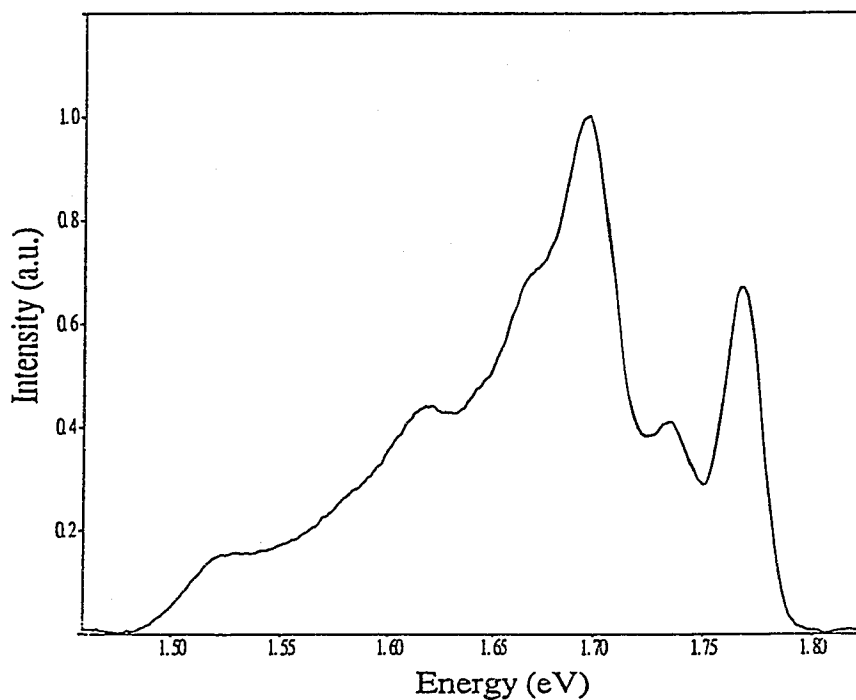
Figure 4.5: PL Spectrum of C_{60} at 10 K

minescence spectrum, and the spot-to-spot variation observed on each sample is less than $\sim 15\%$. The only significant variation in the spectrum that we have observed is controlled by the cooling rate of the crystal from 300 K to 10 K, and will be discussed in a separate subsection.

The theory developed in the preceding section can be applied to C_{60} excimers, resulting in the assignment of the six resolved peaks as follows:

Energy	Wavelength	Initial State
1.767 eV	701.6 nm	E_{1++}
1.735 eV	714.9 nm	E_{1--}
1.696 eV	731 nm	E_{1+-}
1.664 eV	745 nm	E_{1-+}
1.627 eV	761.9 nm	E_{+00}
1.524 eV	813.4 nm	E_{-00}

From (16)

$$E_{1++} - E_{1-+} = 2Ue^{-\gamma} = 1.767 - 1.664 = 0.103eV$$

$$E_{1--} - E_{1+-} = 2Ue^{-\gamma}(1 - 2\gamma) = 1.735 - 1.696 = 0.039eV$$

$$2Ue^{-\gamma}(1 - 2\gamma) = 0.039eV$$

and

$$2Ue^{-\gamma} = 0.103eV.$$

Solving for γ and U we find that

$$\gamma = 0.311 , \quad U = 0.0755eV.$$

From (9):

$$E_{+00} - E_{-00} = 2Ue^{-\gamma} = 1.627 - 1.524 = 0.1.0 = E_{1--} - E_{1+-}$$

so the monomer (U$\sim$0) 0–0 line is

$$\frac{E_{+00}+E_{-00}}{2} = \frac{1.627+1.529}{2} = 1.576eV = E_0 + \hbar\omega_0$$

and the monomer (U$\sim$0) 1–0 line is

$$\frac{E_{1++}+E_{1--}}{2} = \frac{1.767+1.664}{2} = 1.716eV = E_0 + \hbar\omega_0.$$

Monomer emission can be observed to various extents on different films, as evidenced by the 1–0 line at 1.716 eV seen in Figure 4.6.

The vibrational quantum energy is

$$\hbar\omega_0 = 0.140 \text{ eV}.$$

The polaron-exciton binding energy is:

$$E_b = \frac{kc^2}{2} = \gamma\hbar\omega_0 = 0.044 \text{ eV}.$$

Transition probabilities for dimers were calculated by Fulton, et al., [39], who showed exciton splitting for the bimolecular complex and discussed allowed and forbidden
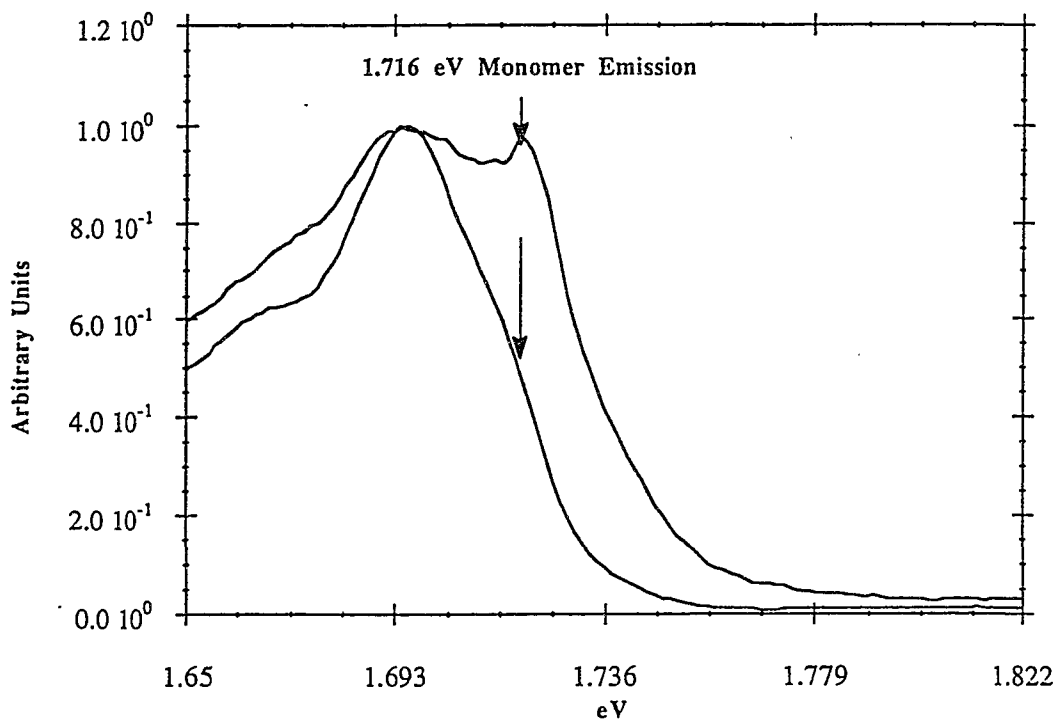
Figure 4.6: PL Data Showing Degrees of $S_1(\nu = 1)$–S_0 Monomer Emission (1.716 eV) for Two Different Films at about 120 K

transitions for various geometries of transition dipole vectors for the two limiting cases of weak and strong electronic coupling.

Let the intensity of a single molecule line be $I_a = |\vec{M}_a|^2$ where the matrix element of the transition dipole is

$$\vec{M}_a = \langle \phi'_a | \vec{D} | \phi_a \rangle.$$

For a transition from the symmetric electronic state

$$\vec{M}_{+\pm} = \tfrac{1}{2} \langle \phi'_a \phi_b (\chi'_{1a}\chi_{0b} \pm \chi'_{0a}\chi_{1b}) + \phi_a \phi'_b (\chi_{0a}\chi'_{1b} \pm \chi_{1a}\chi'_{0b}) | \vec{D} | \phi_a \phi_b \chi_{0a}\chi_{0b} \rangle =$$

$$\tfrac{1}{2} \{ \vec{M}_A (S_{01} \cdot 1 \pm S_{00} \cdot v) + \vec{M}_b (1 \cdot S_{01} \pm v \cdot S_{00}) \} \quad \vec{M}_{+-} = \tfrac{\vec{M}_a + \vec{M}_b}{2} (\sqrt{\gamma} \pm v) e^{\frac{\gamma}{2}}$$

Where $v \equiv \langle \chi_{1a} | \chi_{0a} \rangle = 0$ if we have an orthonormal set of vibrational functions (Hermite polynomials). Due to vibrational coupling of a molecule with the crystal lattice the intermolecular vibrational eigenfunctions may lose their orthonormality. In the same manner:

$$\vec{M}_{-\pm} = \frac{\vec{M}_a - \vec{M}_b}{2} (\sqrt{\gamma}) e^{-\frac{\gamma}{2}} \tag{4.80}$$

For 0-0 transitions, the matrix element is simpler:

$$M_{0\pm} = \tfrac{1}{\sqrt{2}} \langle \phi'_a \phi_b \chi'_{0a}\chi_{0b} \pm \phi_a \phi'_b \chi_{0a}\chi'_{0b} | \vec{D} | \phi_a \phi_b \chi_{0a}\chi_{0b} \rangle =$$

$$\tfrac{1}{\sqrt{2}} (\langle \phi'_a | \vec{D} | \phi_a \rangle \langle \phi_b | \phi_b \rangle \langle \chi'_{0a} | \chi_{0a} \rangle \langle \chi_{0b} | \chi_{0b} \rangle \pm \langle \phi_a | \phi_a \rangle \langle \phi'_b | \vec{D} | \phi_b \rangle \langle \chi_{0a} | \chi_{0a} \rangle \langle \chi'_{0b} | \chi_{0b} \rangle) =$$

$$(\vec{M}_1 S_{00} \cdot 1 \pm \vec{M}_2 1 \cdot S_{00}) \tfrac{1}{\sqrt{2}}$$

$$= S_{00} \frac{\vec{M_1} \pm \vec{M_2}}{\sqrt{2}}$$

$$= e^{-\frac{\gamma}{2}} \frac{\vec{M_a} \pm \vec{M_b}}{\sqrt{2}}$$

Without interaction we have only the single molecule energy $(E_0 + \hbar\omega)$ and transition dipole matrix elements $\vec{M} = \vec{M_a} = \vec{M_b}$. Table 4.3.1 gives the energy and matrix element for each energy level.

Exp. energy (eV)	Calculated energy	Radiation transition prob.
1.767	$E_{1,+,+} = E_0 + 2\,\hbar\omega + Ue^{-\gamma}$	$(\vec{M_a} + \vec{M_b})\frac{\sqrt{\gamma}e^{-\gamma/2}}{2}$
1.735	$E_{1,-,-} = E_0 + 2\,\hbar\omega + Ue^{-\gamma}(1 - 2\gamma)$	$(\vec{M_a} - \vec{M_b})\frac{\sqrt{\gamma}e^{-\gamma/2}}{2}$
1.696	$E_{1,+,-} = E_0 + 2\,\hbar\omega - Ue^{-\gamma}(1 - 2\gamma)$	$(\vec{M_a} + \vec{M_b})\frac{\sqrt{\gamma}e^{-\gamma/2}}{2}$
1.664	$E_{1,-,+} = E_0 + 2\,\hbar\omega + Ue^{-\gamma}$	$(\vec{M_a} - \vec{M_b})\frac{\sqrt{\gamma}e^{-\gamma/2}}{2}$
1.627	$E_{0,+} = E_0 + \hbar\omega + Ue^{-\gamma}$	$(\vec{M_a} + \vec{M_b})\frac{e^{-\gamma/2}}{\sqrt{2}}$
1.524	$E_{0,-} = E_0 + \hbar\omega - Ue^{-\gamma}$	$(\vec{M_a} - \vec{M_b})\frac{e^{-\gamma/2}}{\sqrt{2}}$

In short, we are proposing that C_{60} forms excited state dimers in the solid. Further, the well structured luminescence emitted from solid C_{60} can be explained in terms of splitting of these degenerate excimeric states. The singlet state potential well contains $v=0$ and $v=1$ vibrational states, which are split into a doublet and a quartet of states due to the electronic-vibrational mixing. We have illustrated the potential energy of this bimolecular complex, with the ground state and lower excited states, using a configurational coordinate Q, shown in Figure 4.7.
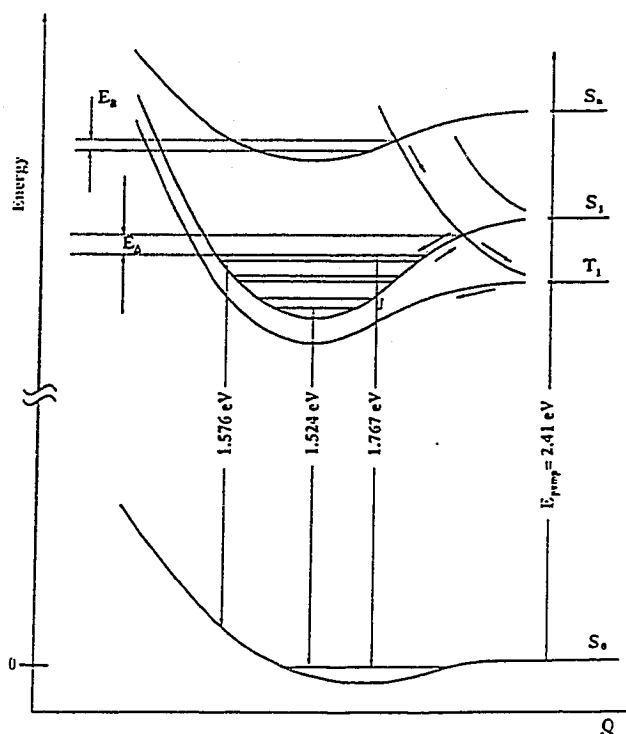
Figure 4.7: Excimeric States and Their Splitting, Illustrated Along Configurational Coordinate, Q

It is possible to attribute some limited physical character to this coordinate. The configuration coordinate Q could be envisioned as the distance between the closest carbon nuclei from neighboring molecules, one belonging to one of the pentagon apices, the other to the edge of a double bond of the adjacent molecule, in the *P-configuration*. This configuration corresponds to an alignment of molecules such that an electron rich double bond of one molecule faces an electron poor region in the center of a pentagon on the adjacent molecule. In this manner, the internal and external vibrations are linked to one another for temperature ranges in which the rotational and

vibrational motions are frozen (90-150K). Matus, et al., states that the temperature dependence of the luminescence is correlated with the degree of rotational disorder, and for rotating molecules we can expect the configurational coordinate Q to approach infinity. Since the ground state molecules are held together weakly, only a shallow minimum with a single vibrational level is expected for the ground state potential curve of the C_{60} dimer. Note that the excited state minimum is shifted by c from that of the ground state. In the Friedman-Harigaya model, the excited state shift is c= 0.0125 Å and is attributed to the intramolecular dimerization. The bond length between a pentagon and a hexagon is 1.45 Å while between two hexagons (h-h) it is 1.40 Å. This yields an average length of 1.425 Å. To come to this average value, each carbon nucleus of the (h-h) bond must be displaced .0125 Å.

The approximation of the nuclear motion as one dimensional oscillation is crude, but can be justified for C_{60} by the fact that only $A_g(2)$ and $H_g(8)$ modes are intense in the Raman spectrum and by the fact that a similar model used by Friedman and Harigaya gives a good description for a single C_{60} molecule. In Figure 4.7, the triplet potential curve is shown split, in analogy with rare gas excimers, and the triplet state T_1 has a bound state energy lower than the bound state of S_1. The minimum of the singlet potential well is shifted from the minimum of the ground state potential due to

the intermolecular electronic coupling in the excited state (in the harmonic approx-

imation, this yields the Frank-Condon overlap integrals), as previously mentioned.

Comparison with experimental peaks in the fluorescence spectra for low tempera-

tures gives: $\gamma = 0.31$, $U = 0.075$ eV, $E_0 = 1.576$ eV and $\hbar\omega = 0.140$ eV. The four

parameters γ, U, E_0, and $\hbar\omega$ enable us to describe the 6 peaks which characterize the

luminescence spectrum of crystalline C_{60}.

A theoretical fit to the experimental photoluminescence spectra is plotted in

Figure 4.8. For the single crystal data at 10 K the six bound-to-bound transitions ob-
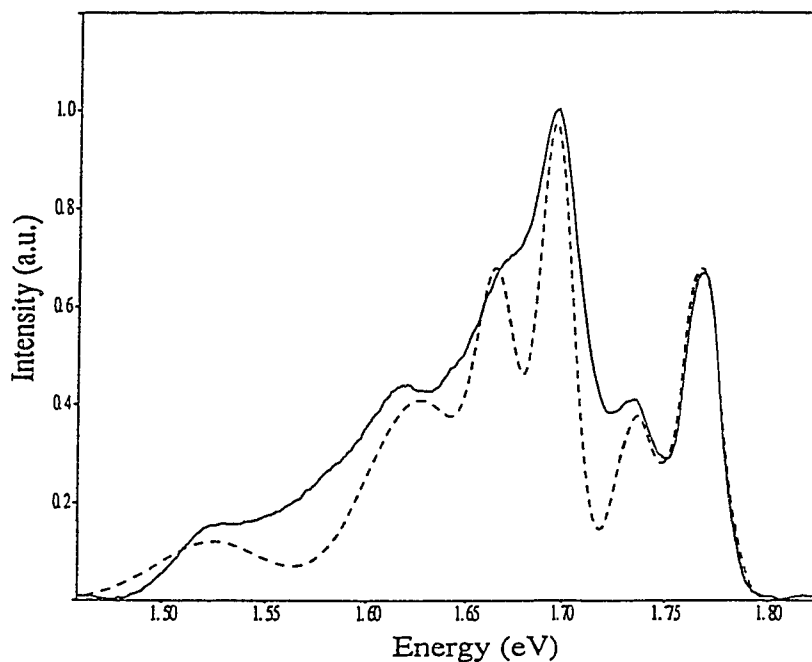

Figure 4.8: PL Spectrum of Crystalline C_{60} at 10 K (Solid Line), and Theoretical Fit

tained from our model are shown superimposed on the experimental spectrum. This fit was obtained using peak widths of 0.014 eV for the 1-0 transitions, and 0.035 eV for the 0-0 transitions. The peak height ratios obey the following relations:

$$\frac{I(1.767)}{I(1.716)}(T < 70K) \approx \frac{I(1.696)}{I(1.664)}(T < 130K) \approx \frac{I(1.627)}{I(1.524)}(T < 130K) \approx 1.6 \quad (4.81)$$

These peak ratios are well described by the ratio of dipole transition matrix elements:

$$\frac{|\vec{M}_a + \vec{M}_b|^2}{|\vec{M}_a - \vec{M}_b|^2} = \frac{\vec{M}_a^2 + \vec{M}_a \cdot \vec{M}_b}{\vec{M}_a^2 - \vec{M}_a \cdot \vec{M}_b}. \quad (4.82)$$

where

$$\vec{M}_a = \langle \phi_a' | \vec{D} | \phi_a \rangle \quad (4.83)$$

For instance

$$\vec{M}_{0\pm} = \frac{1}{\sqrt{2}} \langle \phi_a' \phi_b \chi_{0a}' \chi_{0b} \pm \phi_a \phi_b' \chi_{0a} \chi_{0b}' | \vec{D} | \phi_a \phi_b \chi_{0a} \chi_{0b} \rangle.$$

See table 4.3.1 for all relevant dipole matrix elements.

4.3.2 Thickness Dependence

Though our model considers only dimers, we have been able to verify the bulk origin of all of the peaks in the observed C_{60} PL spectrum, in contrast to the work of Guss,

et al., [10]. In order to determine this, films were grown of several different thicknesses

between 200 Å and 10000 Å. The absorption depth of C_{60} at the excitation wavelength

of 514 nm is approximately 3300 Å [40]. Suppose it were the case that certain peaks

in the spectrum are due to surface induced mechanisms while others were due to bulk

mechanisms; then spectra from C_{60} films of greatly different thicknesses would show

large changes in the amplitudes of surface induced peaks relative to the amplitudes of

bulk induced peaks. Figure 4.9 shows the normalized spectra obtained from two films

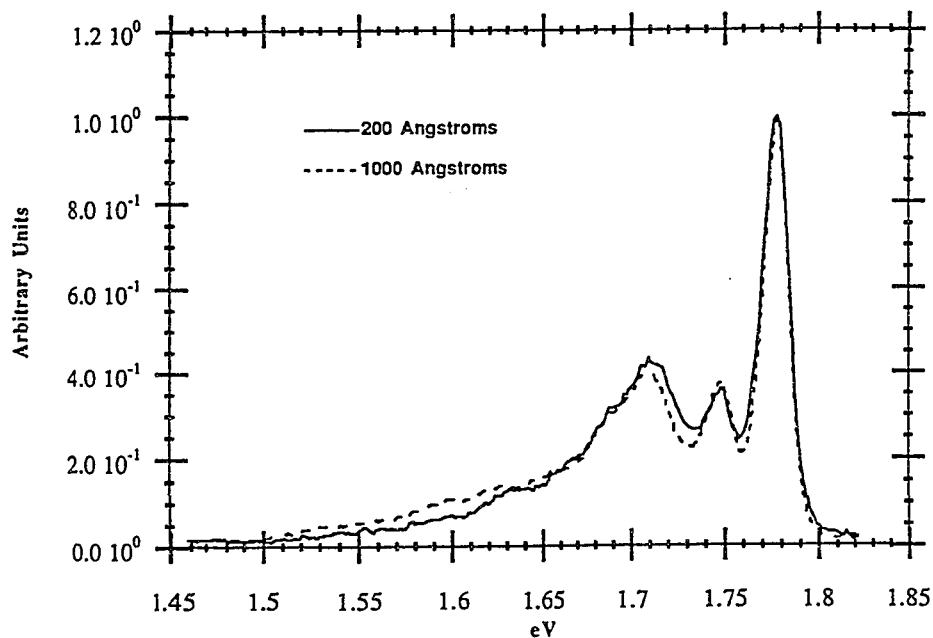of different thicknesses. Figure 4.10 shows the non-normalized PL spectra of films

Figure 4.9: Normalized PL Spectra Taken of Two Films of Different Thicknesses

of 200, 1000, and 10,000 Å thickness. The spectral peak heights are approximately proportional to the film thickness, indicating that the photoluminescence spectral features result from bulk processes alone. In Figure 4.11, the integrated intensity of the PL spectrum of each film is plotted as a function of film thickness, along with a fit of the form

$$I = A(1 - e^{\frac{T_F}{T_{crit}}}) \tag{4.84}$$

where T_F is the film thickness, and A is a parameter which takes into account the quantum efficiency and collection efficiency of our photoluminescence appara-
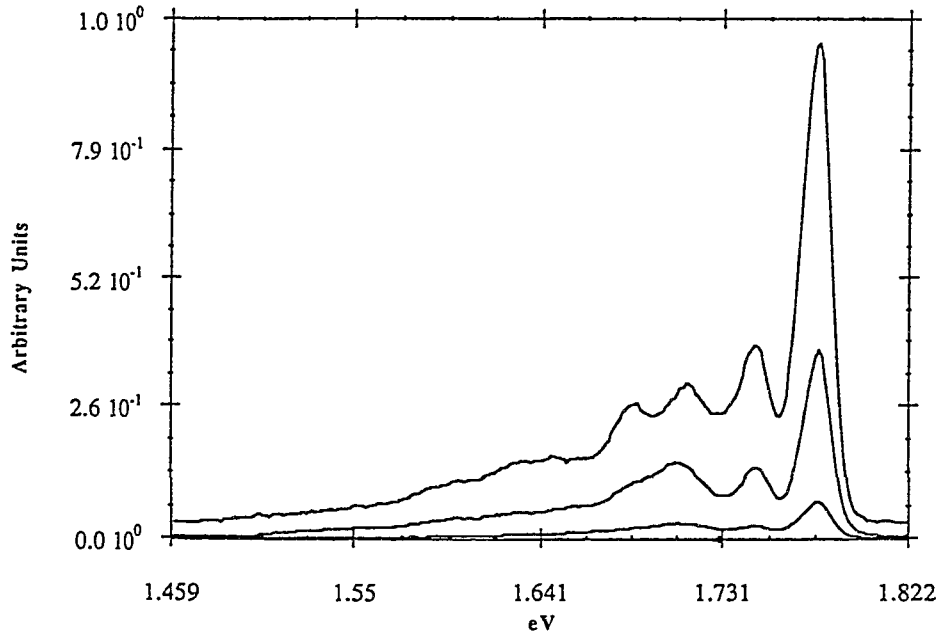
Figure 4.10: PL Spectra of Films of 200 Å, 1000 Å, and 10,000 ÅThickness

tus. From fitting the photoluminescence integrated intensity to this functional form,

T_{crit} is found to be 1620 Å.

We take into account that the Sb substrate is highly reflective at the excitation

wavelength, and that the incident radiation must pass through the film a second time

upon reflection from the substrate. Thus, if the entire PL spectrum of C_{60} is due to

processes of a bulk nature, we would expect that

$$T_{crit} = \frac{D}{2} \tag{4.85}$$

Figure 4.11: PL Integrated Intensity vs. Film Thickness
With Fit of Form $I = A(1 - e^{\frac{T_F}{T_{crit}}})$

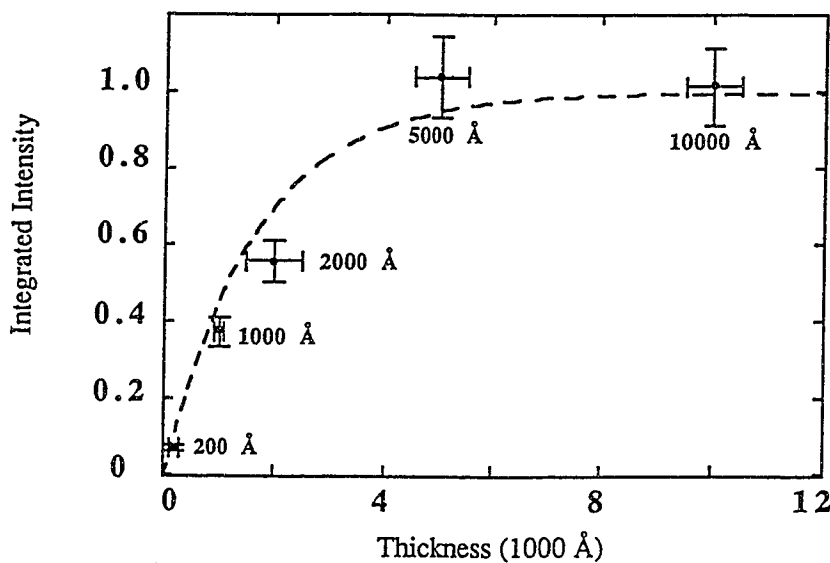where D is the absorption depth of C_{60} at 514 nm. This simple analysis, based on the Beer-Lambert absorption law, implies that T_{crit} should be approximately 1650 Å, in excellent agreement with the value of 1620 Å that we find experimentally. This finding further indicates that all of the features in the C_{60} photoluminescence spectrum originate from the bulk.

4.3.3 Cooling Dependence

Spectra for films cooled at different rates differ in the magnitude of the two highest energy peaks compared to the rest of the spectrum. Figure 4.12(a) and (b) depict the two types of PL spectra that we observed from thin film crystalline C_{60}, normalized to the highest peak in each spectrum. Spectrum (a) is obtained after cooling the sample rapidly, at a rate of approximately 5 K min^{-1}. Spectrum (b) is the result of much slower cooling, at an average rate of about 0.5 K min^{-1}. In the second case, the rate of cooling was not constant; the temperature was lowered in steps of 20 K to allow the photoluminescence to reach equilibrium at each temperature, starting at 290 K. Although peaks appear at approximately the same energies in both the fast cooled and slow cooled spectra, there are noticeable peak height differences. Because there are phase transitions in C_{60} that have a time constant on the order of several
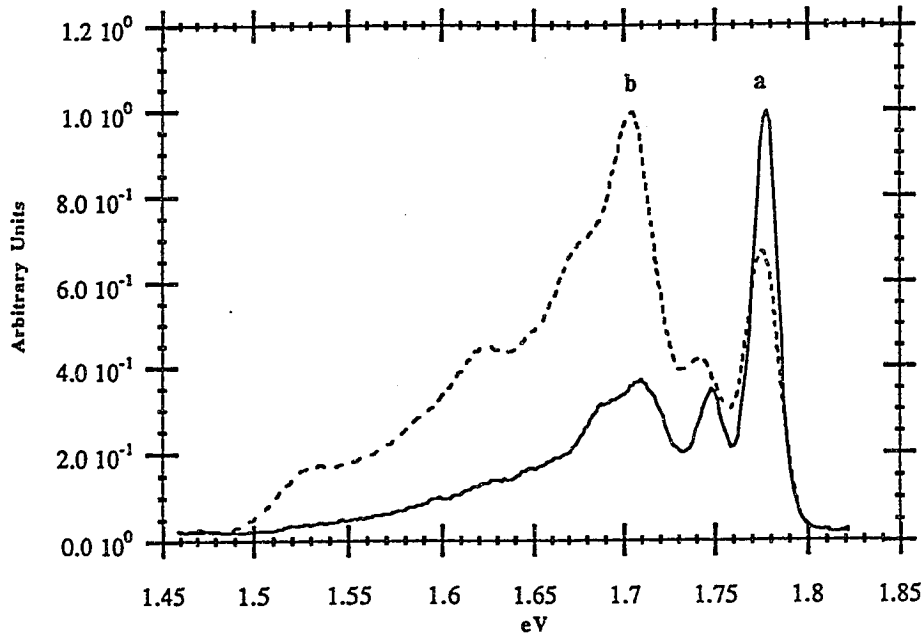
Figure 4.12: Cooling Rate Dependence of PL Spectrum
(a)quickly cooled and (b)slowly cooled.

hours [34], we propose that the fast cooled spectrum is the direct result of cooling

through these phase transitions without allowing time for the sample structure to

adjust. This is known as *supercooling*. The supercooling phenomenon and its effect

on the luminescence spectrum has been been previously studied in pyrene [41]. The

luminescence from equilibrium cooled pyrene is found to contain two pronounced

features centered at about 375 nm and 460 nm. Picosecond time resolved studies

performed at room temperature show that shortly after excitation the emission at

375 nm begins decreasing while the emission at 460 nm increases. The authors of
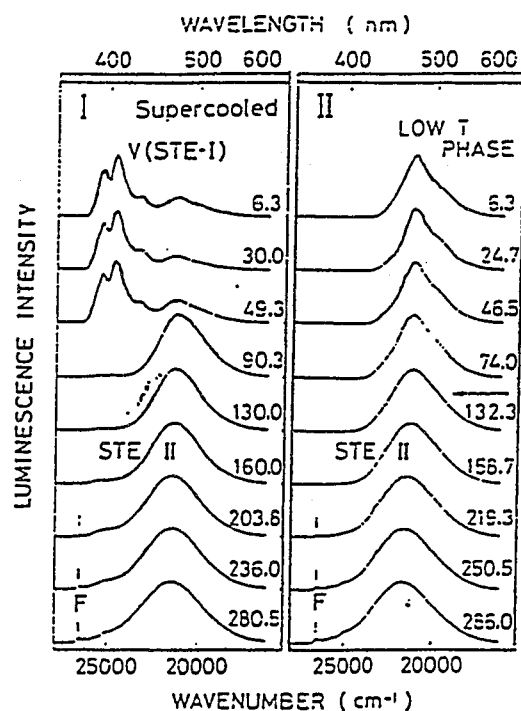
Figure 4.13: Supercooling in Pyrene
from Matsui, et al. [42]

that work interpret this to indicate decay of a free exciton at 375 nm and decay of

a self-trapped exciton at 460 nm. The time dependent behavior was attributed to

energy migration across an adiabatic potential barrier, from the free exciton state

to the self-trapped exciton state. When a similar pyrene crystal was supercooled

through the pyrene phase transition at 120 K the spectrum contained, in addition

to the features previously noted, structured emission in the energy region between

the free exciton and self-trapped exciton regions. This additional luminescence was

attributed to a new self-trapped exciton state created by lattice distortion that may have occured as a result of supercooling.

One problem with the multi-well interpretation of the pyrene slow-cooled and supercooled luminescence spectra is that this view requires decreasing rates of crossing to the self-trapped exciton state with decreasing temperature. In fact, it has been shown that in pyrene this rate increases with decreasing temperature [42]. This difficulty is overcome by assuming a by-pass process similar to that proposed for solid Xe [43], in which the system may pass directly to the self-trapped exciton state without first relaxing to the free-exciton state. Thus while the rate of crossing from the free exciton state to the self-trapped exciton state decreases with decreasing temperature, the rate of by-pass relaxation may increase, allowing the multi-well picture to fit the pyrene luminescence data.

The distinct luminescence spectrum of supercooled crystalline pyrene may be analogous to the spectrum we observe upon rapidly cooling thin film crystalline C_{60}. Time resolved luminescence spectra of room temperature pyrene show transient features in the energy region where the additional supercooled features appear at low temperatures. This could indicate that the energy states responsible for the supercooled pyrene spectrum actually exist at room temperature. If this is the case, then it is

plausible that these states appear in the spectrum as unrelaxed luminescence from higher excited states of pyrene excimers. The ordinary pyrene luminescence has been attributed to excimer decay from the *excimer state* [41]. (It has been shown that unrelaxed luminescence occurs with some small quantum efficiency in many aromatic molecules [44, 45, 46, 47, 48].) Because C_{60} molecules have high rotational energy at room temperature, it is not expected that time resolved room temperature luminescence spectra would show anything but monomer emission. At temperatures at which the C_{60} molecules begin to correlate with each other, the solid pyrene and solid C_{60} systems may be analogous. The existance of the supercooled spectra may be due to a lattice distortion or strain which affects the rates of internal conversion from higher excited excimer states down to the first excited state, causing a high rate of unrelaxed luminescence [27]. In addition to this, a lattice distortion could affect the height of the barrier to thermal depopulation to the triplet state. Either of these phenomena would cause spectral variations similar to those observed upon supercooling pyrene and C_{60}.

X-ray diffraction studies of solid C_{60} have used extinction factors to study the glassy phase of C_{60} [34]. These studies determined that there is a finite relaxation time for molecular reorientation upon cooling below 90K. This relaxation occurs as

the formation of clusters of space group $P2_13$ in a matrix of space group $Pa3$. The matrix slowly becomes completely $P2_13$. The relaxation time corresponding to the cooling rates and final temperatures used in our work can be estimated from the work of Toyoda, et al., [34] to be on the order of several days. Clearly if our model for the luminescence of C_{60} is correct, then this orientational clustering in the fast cooled case may be leading to an inhibition to the depopulation of the highest vibrational level in the first singlet state. The distortion of the barrier to intersystem crossing would need to be on the order of 10% in order to cause the observed intensity variations in the PL spectra.

4.3.4 Polycrystalline C_{60} Thin Film

In contrast to the PL spectrum observed for crystalline thin film C_{60}, the polycrystalline thin film C_{60} photoluminescence spectrum at 10 K, shown in Figure 4.14, exhibits a single large but asymmetric peak centered at about 1.687 eV. This is accompanied by a broad low-energy shoulder.

Although the peak positions predicted by our model are used to obtain an acceptable fit to the PL spectrum of polycrystalline C_{60}, as shown in Figure 4.14, there are several noticeable discrepencies between the fit and the data. The aspects
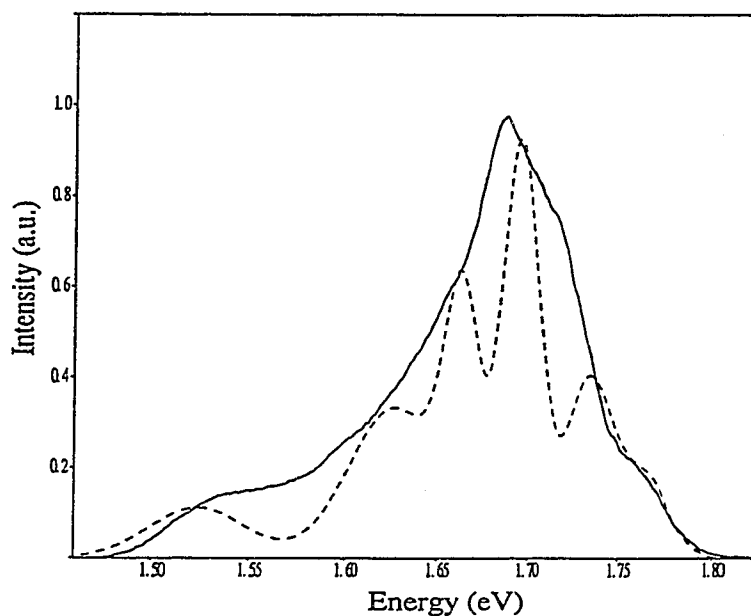
Figure 4.14: PL Spectrum of Polycrystalline C_{60} Taken at 10 K (Solid Line) and Six-gaussian Fit Using Peak Positions Used for Crystalline PL Fit

where the polycrystalline data diverge from our crystalline model are the additional intensity at 1.576 eV, the absence of a peak at 1.767 eV, the shift of the 1.696 eV peak to lower energy, and the overall broadening of the spectral features. The wide range of local environments due to small domain size ($\sim 100\text{Å}$ domain size) in the polycrystalline material may be the cause of these discrepencies. It is plausible that the varying molecular environments would lead to inhomogeneous broadening of all of the radiative transitions we observe. Furthermore, in the same way that a highly crystalline structure would tend to enhance the formation of excimers and exciplexes,

a polycrystalline structure may lead to a greater number of molecules not strongly associated with any other molecule. This would be seen as an increase in monomer emission from the lowest vibrational state in the S_1 manifold to the bottom of the S_0 manifold. This transition has an energy of 1.576 eV, and can be seen to be enhanced in the polycrystalline spectrum. Monomer emission should also be observable from the first excited vibrational state in the S_1 manifold to the bottom of the S_0 manifold. This transition has an energy of 1.716 eV and is also observed in the polycrystalline spectrum.

The shift in the 1.696 eV peak and the drastic change in intensity of the two highest energy features is likely caused by strain in the polycrystalline sample. It has been reported for similar systems that strain in the material can modify the intersystem crossing rate (S_1-T_1) and the triplet state lifetime [49]. If a lowering of the intersystem crossing barrier occurred in polycrystalline C_{60}, the states with the lowest barriers would be preferentially affected. Thus it is possible that a change in the barrier to intersystem crossing is occurring in polycrystalline C_{60} and affects most strongly the dimeric level which is at 1.767 eV in the crystalline sample. This is the level with the lowest barrier to intersystem crossing. The absence of features from this level in the polycrystalline PL spectrum can then be attributed to a high rate

of intersystem crossing from this excited state, effectively decreasing the population there. The strong decrease in the luminescence observed at 1.735 can be attributed to the same phenomenon with the added observation that the PL intensity at this energy is affected less strongly than that at 1.767 eV due to a greater barrier height. A change of the intersystem crossing barrier could mean that the average shape of the S_1 well near the barrier is different in polycrystalline C_{60} than in crystalline C_{60}. This would explain the shift in energy of the 1.696 eV peak. (Such a shift should also be present for the 1.735 eV peak, but is not clearly resolvable due to the low intensity of the the feature.)

4.4 Temperature Dependence of C_{60} PL

4.4.1 Single Crystal Thin Film C_{60} Temperature Dependence

Figure 4.15 shows the evolution of the photoluminescence spectrum as a function of temperature. As expected, the peaks broaden as a function of increasing temperature, and the peaks decrease in intensity. In order to more fully understand the temperature dependence of the PL spectrum, we apply a rate equation approach to various energy transfer mechanisms in the dimeric system. The excited singlet vibronic states are quenched through radiative decay at a constant radiative decay rate of τ^{-1} and a

nonradiative de-excitation channel stemming from the crossing of potential terms, also known as inter-system crossing. The energy flowing across the inter-system crossing barrier of energy E_i has a temperature dependence given by the following transition rate:

$$\nu = \nu_i e^{-\frac{E_i}{k_B T}}. \tag{4.86}$$

Pumping of the vibronic states occurs through the dimer formation from a radiatively excited C_{60} molecule, at a rate $N_0 P$, where N_0 is the density of ground state molecules and P is the pumping rate.
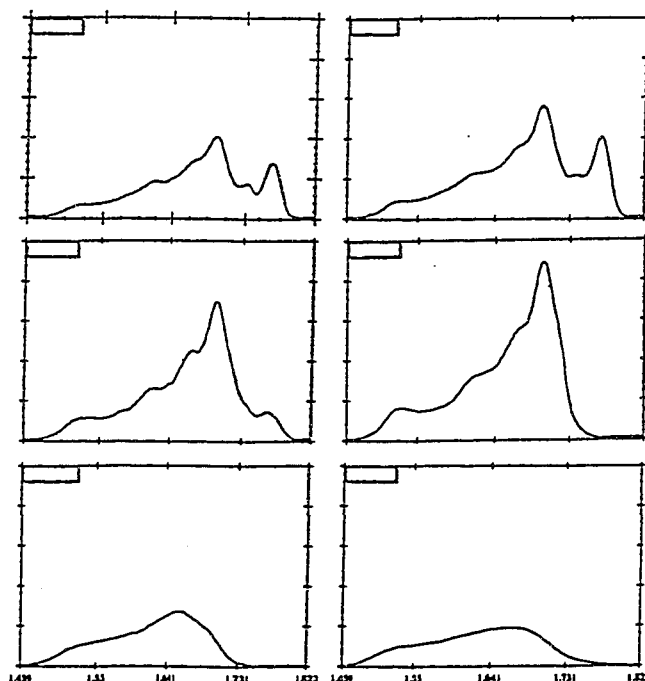

Figure 4.15: C_{60} PL Temperature Dependence

Pumping also occurs through the higher lying excitons, such as more complex excitons and free excitons connected to the crystal lattice. In this case, the free exciton must overcome an energy barrier E_B , analagous to the "self-trapping barrier" discussed in [8] to relax to a state from which radiative decay can occur. The resultant balance equation for a vibronic state is:

$$\frac{dN_i}{dt} = N_0 P + N_0 P \kappa e^{-\frac{E_B}{k_B T}} - \frac{N_i}{\tau_R} - N_i \nu_i e^{-\frac{E_i}{k_B T}} \qquad (4.87)$$

During CW pumping, the steady state luminescence is described by:

$$I_{lum} = N_i \tau_R^{-1} = N_0 P \frac{1 + \kappa e^{-\frac{E_B}{k_B T}}}{1 + \tau_R \nu_i e^{-\frac{E_i}{k_B T}}} \qquad (4.88)$$

By fitting the peaks of the decomposed PL temperature spectra to this functional form between 0 K and 150 K we find that $E_B = 0.012$ eV and $\overline{\kappa} = 4.0$ for the six lines from the levels $E_{0,1;\pm\pm}$. For the singlet vibrationally excited levels the magnitudes of the quenching barriers found from the fit are 0.068, 0.100, 0.138, and 0.170 eV given from highest to lowest states. These values, together with the radiative transition energy give the absolute energy between the ground state and the crossing of the singlet and triplet potential curves to be 1.835 eV. We can calculate the energy difference between the minimum of the excited potential and the ground state as $E_0 - \hbar\omega = 1.576$ eV $-.070$ eV $= 1.506$ eV, so the depth of the well is $1.835 - 1.506 = 0.329$ eV. Assuming

that the ground electronic state and the excited electronic state have approximately the same spring constant, the $v = 0$ state of the ground electronic state will be at around 0.070 eV above the bottom of the well. Since the sublimation temperature of solid C_{60} has been experimentally found to be about 650 K, the depth of the ground state well for a system of two unexcited C_{60} molecules can be estimated at 56 meV. Due to the fact that the level of the $v = 0$ state and the depth of the well are on the same order, it is reasonable to assume that there is only one vibrational level in the electronic ground state. From our fit of the spectral data to gaussians, we take the widths to find ν_i for each peak. Using the fit to the temperature dependence of the amplitudes of the spectral peaks, the value of the coefficient $\tau_R \nu_i$ can be inferred. The values of τ_R verify the prediction that the $(\vec{M}_a + \vec{M}_b)$ transition is more probable than the $(\vec{M}_a - \vec{M}_b)$ transition. The overall radiative lifetime is found to be:

$$\tau_{\text{effective}} = (\sum_i \frac{1}{\tau_i})^{-1} = 0.91 \text{ ns} \qquad (4.89)$$

4.4.2 Polycrystalline Thin Film Temperature Dependence

An equilibrium rate equation approach has been applied previously to the photo-luminescence spectrum of polycrystalline C_{60} [8]. A model similar to the model in Matsui, et al. [42] was proposed in which the first excited singlet state is pumped

by direct processes as well as by the conversion of free excitons to the self-trapped exciton state. The resultant functional form for the temperature dependence of the integrated spectral intensity is

$$\eta(T) = \frac{c_0 + c_1 exp(\frac{E_1}{k_B T})}{1 + c_2 exp(\frac{E_2}{k_B T})} \tag{4.90}$$

where T is the temperature and k_B is Boltzmann's constant. In that study, E_B (E_1) was found to be .010 eV and E_i (E_2) was found to be 0.172 eV. These values are in very good agreement with the values found in our study. We observe the mean barrier to intersystem crossing to be 0.138 eV. Because the peaks in the polycrystalline data are difficult to resolve due to the effects mentioned above, the barrier to intersystem crossing obtained must be treated as an effective barrier for the whole vibrational manifold of S_1. The barrier for self-trapped exciton formation should, however, be analagous to that found for crystalline C_{60}. This is, in fact, very nearly the case, as the barrier to the self-trapped exciton averages 0.013 eV in our studies of crystalline C_{60}.

4.5 Summary

This chapter establishes the basic concepts underlying luminescence of many organic molecules. It further attempts to explain the luminescence of crystalline C_{60} in light

of these concepts, through the use of a conceptually simple model. The system that is used to model the process of luminescence in crystalline C_{60} is an excimer model, whereby two molecules become associated upon the excitation of one of them. This association and the resulting wave function overlap causes splitting of the degenerate vibrational states in the first excited electronic level. The degree of splitting depends upon the degree of overlap, and for certain values, agrees very well with the observed crystalline C_{60} PL spectrum. Additionally, we used the model to calculate the expected intensity ratios for the different spectral features, and the results are also in good agreement with the data. Temperature dependences of the various peaks were obtained through an equilibrium rate equation approach, and the results further support the validity of our explanation. The model also explains the observed dependence of the luminescence on film thickness and on cooling rate. Our model, with only slight modifications, also predicts the photoluminescence of polycrystalline C_{60}. This is reasonable considering that the only difference between crystalline and polycrystalline C_{60} is the domain size in each.

Chapter 5

Conclusions and Future Directions

There is much to be done before a thorough understanding of the energetics in single crystal C_{60} is obtained. Extension of my work to time resolved photoluminescence of thin film crystalline C_{60} should provide an improved understanding of excited carrier migration and decay, as well as a more detailed analysis of internal conversion and intersystem crossing. Time-resolved photoluminescence measurements have been made on C_{60}, both in solution and in the solid state [50, 51, 52]. However, these studies did not track individual peaks but rather the integrated spectrum, or individual peaks with the implicit assumption that the time dependence of all the peaks would be the same. The well-structured nature of the photoluminescence emitted from our thin film crystalline C_{60} should allow for accurate measurement of the time depedence of the excited states underlying each peak. Measurements of the time behavior of each peak could verify our assignments of the peaks. Photoluminescence studies using lower excitation energies should prove helpful in verifying our model. Studies using excitation energies between the excimeric states of $S_1(\nu = 0)$ and $S_1(\nu = 1)$

should show an absence of transitions from the $S_1(\nu = 1)$ state. It may be possible to selectively excite states up to a certain level within the S_1 manifold. Such experiments performed at different temperatures will allow a better understanding of the energy partitioning between various vibrational levels in the excited electronic state.

Due to the large coherence length present in these highly crystalline films, they may be useful in determining the extent to which effects due to domain boundaries and disorder may have affected earlier studies. For instance, preliminary transient absorption studies to determine the rate of intersystem crossing in pure and solvated polycrystalline C_{60} have hinted that the rates measured may be convolutions of structural and molecular effects. With its well characterized structure, crystalline C_{60} should prove useful in determining if this is the case.

In addition to experiments which bear directly on the photoluminescence studies done for this work, there are other interesting experiments to be performed using single crystal C_{60}. Studies have indicated that the presence of impurities in solid C_{60} can lead to site induced disorder [53]. Thus, samples of slightly doped crystalline C_{60} could be used to investigate the effects of a certain degree of disorder on the optical properties of the solid. This could allow for a more complete determination of the role of grain bounderies and the crystal field in energy transfer and migration.

Bibliography

[1] K. Sinha, J. Menendez, R. C. Hanson, G. B. Adams, J. B. Page, and O. F. Sankey, Chem. Phys. Lett. **186**, 287 (1991).

[2] M. P. Joshi, S. R. Mishra, H. S. Rawat, S. C. Mehendale, and K. C. Rustagi, Appl. Phys. Lett. **62**, 1763 (1993).

[3] Z. H. Kafafi, J. R. Lindle, R. G. S. Pong, F. J. Bartoli, L. J. Lingg, and J. Milliken, Chem. Phys. Lett. **188**, 492 (1992).

[4] N. S. Sariciftci, D. Braun, C. Zhang, V. I. Srdanov, A. J. Heeger, G. Stucky, and F. Wudl, App. Phys. Lett. **62**, 585 (1993).

[5] R. C. H. et al, Nature **350**, 320 (1991).

[6] A. F. Hebard, Physics Today , 26 (1992).

[7] M. J. Rosseinsky, A. P. Ramirez, S. H. Glarum, D. W. Murphy, R. C. Haddon, A. F. Hebard, T. T. M. Palstra, A. R. Kortan, S. M. Zahurak, and A. V. Makhija, Phys. Rev. Lett. **66**, 2830 (1991).

[8] R. D. Averitt, C_{60} purification and C_{60} film characterization, Master's thesis, Rice University, 1994.

[9] M. R. Fraelich and R. B. Weisman, J. Phys. Chem. **97**, 11145 (1993).

[10] W. Guss and J. F. et al, Phys. Rev. Lett. **72**, 2644 (1994).

[11] G. V. Tendeloo, et al., J. Phys. Chem. **96**, 7424 (1992).

[12] D. E. Luzzi, J. E. Fischer, X. Q. Wang, D. A. Ricketts-Foot, A. R. McGhie, and W. J. Romanow, J. Mater. Res. **7**, 335 (1992).

[13] M. S. Dresselhaus, G. Dresselhaus, and P. C. Eklund, J. Mater. Res. **8**, 2054 (1993).

[14] D. S. Bethune, R. D. Johnson, J. R. Salem, M. de Vries, and C. S. Yannoni, Nature **366**, 123 (1993).

[15] A. Ito, T. Morikawa, and T. Takahashi, Chem. Phys. Lett. **211**, 333 (1993).

[16] J. A. Dura, P. M. Pippenger, N. J. Halas, X. Z. Xiong, P. C. Chow, and S. C. Moss, Appl. Phys. Lett. **63**, 3443 (1993).

[17] W. I. F. David, R. M. Ibberson, T. J. S. Dennis, J. P. Hare, and K. Prassides, Europhysics Letters **18**, 219 (1992).

[18] J. A. Dura, J. T. Zborowski, and T. D. Golding, Mater. Res. Soc. Symp. Proc. **263**, 35 (1992).

[19] R. D. Averitt and N. J. Halas, Appl. Phys. Lett. **65**, 374 (94).

[20] L. C. Feldman and J. W. Mayer, *Fundamentals of Surface and Thin Film Analysis*, North-Holland, 1986.

[21] J. A. Dura, A. Vigliante, T. D. Golding, and S. C. Moss, (unpublished).

[22] M. A. VanHove, W. H. Weinberg, and C. M. Chan, *Low-Energy Electron Diffraction*, Springer-Verlag, 1986.

[23] M. V. Heimendahl, *Electron Microscopy of Materials, an Introduction*, Academic Press, 1980.

[24] C. Kittel, *Introduction to Solid State Physics*, John Wiley and Sons, Inc., 6 edition, 1986.

[25] P. W. Stephens, L. Mihaley, P. L. Lee, R. L. Whetten, S. M. Huang, R. Kaner, F. Diederich, and K. Holczer, Nature **351**, 632 (1991).

[26] P. A. Heiney, J. E. Fischer, A. R. McGhie, and W. J. Romanow, Phys. Rev Lett. **67**, 1468 (1991).

[27] M. D. Lumb, *Luminescence Spectroscopy*, Academic Press, 1978.

[28] T. Förster, *Modern Quantum Chemistry part III*, page 93, Academic Press Inc., 1965.

[29] W. Siebrand, J. Chem. Phys. **40**, 2223 (1964).

[30] W. T. Simpson and D. L. Peterson, J. Chem. Phys. **26**, 588 (1957).

[31] D. S. McClure, Can. J. Chem. Phys. **36**, 59 (1958).

[32] E. G. McRae, Austral. J. Chem. **14**, 329 (1961).

[33] E. G. McRae, Austral. J. Chem. **16**, 295 (1963).

[34] N. Toyoda, K. Sakaue, H. Terauchi, T. Arai, Y. Murakami, and H. Suematsu, Journ. Phys. Soc. Jap. **63**, 2025 (1994).

[35] P. H. M. van Loosdrecht, P. J. M. van Bentum, and G. Meijer, Phys. Rev. Lett. **68**, 1176 (1992).

[36] M. Sprik, A. Cheng, and M. Klein, Journal of Physical Chemistry **96**, 2027 (1992).

[37] C. Z. Wang, C. H. Xu, C. T. Chan, and K. M. Ho, J. Phys. Chem. **96**, 3563 (1992).

[38] P. A. Lane, L. S. Swanson, Q.-X. Ni, J. Shinar, J. P. Engel, T. J. Barton, and L. Jones, Phys. Rev. Lett. **68**, 887 (1991).

[39] R. L. Fulton and M. Couterman, J. Chem. Phys. **35**, 1059 (1961).

[40] S. L. Ren et al., Appl. Phys. Lett. **59**, 2678 (1991).

[41] K. Mizuno and A. Matsui, Journal of Luminescence **38**, 323 (1987).

[42] A. Matsui, M. Furukawa, K. Mizuno, and N. T. amd Iwao Yamakazi, Journal of Luminescence **45**, 269 (1990).

[43] E. Roick, R. Gaethke, G. Zimmerer, and P. Gortler, Solid State Commun. **47**, 333 (1983).

[44] T. A. Gregory, F. Hiriyama, and S. Lipsky, J. Chem. Phys. **58**, 4697 (1973).

[45] F. Hirayama, T. A. Gregory, and S. Lipsky, J. Chem. Phys. **58**, 4696 (1973).

[46] D. Huppert, P. M. Rentzepis, and J. Jortner, Chem. Phys. Lett. **13**, 225 (1972).

[47] D. Huppert, P. M. Rentzepis, and J. Jortner, J. Chem. Phys. **56**, 5826 (1972).

[48] P. M. Rentzepis, J. Jortner, and R. P. Jones, Chem. Phys. Lett. **4**, 599 (1970).

[49] C. Kryschi, et al, J. Chem. Phys. **161**, 485 (1992).

[50] A. Andreoni, M. Bondani, and G. Consolati, Phys. Rev. Lett. **72**, 844 (1994).

[51] H. J. Byrne, W. Maser, W. W. Ruhle, A. Mittelbach, W. Honle, H. G. V. Schnering, B. Movagar, and S. Roth, Chem. Phys. Lett. **204**, 461 (1993).

[52] J. Feldmann, R. Fischer, E. O. Gobel, and S. Schmitt-Rink, Phys. Stat. Sol.(b) **173**, 339 (1992).

[53] K. Harigaya, Phys. Rev. B **48**, 2765 (1993).